NONLINEAR CONTROL OF LINEAR PARAMETER VARYING SYSTEMS WITH
APPLICATIONS TO HYPERSONIC VEHICLES

By

ZACHARY DONALD WILCOX

A DISSERTATION PRESENTED TO THE GRADUATE SCHOOL
OF THE UNIVERSITY OF FLORIDA IN PARTIAL FULFILLMENT
OF THE REQUIREMENTS FOR THE DEGREE OF
DOCTOR OF PHILOSOPHY

UNIVERSITY OF FLORIDA

2010

This work is dedicated to my parents, family, friends, and advisor, who have provided me with support during the challenging moments in this dissertation work.

ACKNOWLEDGMENTS

TABLE OF CONTENTS

LIST OF TABLES

LIST OF FIGURES

Abstract of Dissertation Presented to the Graduate School
of the University of Florida in Partial Fulfillment of the
Requirements for the Degree of Doctor of Philosophy

NONLINEAR CONTROL OF LINEAR PARAMETER VARYING SYSTEMS WITH
APPLICATIONS TO HYPERSONIC VEHICLES

By

Zachary Donald Wilcox

August 2010

Chair: Warren E. Dixon
Major: Aerospace Engineering

The focus of this dissertation is to design a controller for linear parameter varying
(LPV) systems, apply it specifically to air-breathing hypersonic vehicles, and examine the
interplay between control performance and the structural dynamics design. Specifically a
Lyapunov-based continuous robust controller is developed that yields exponential tracking
of a reference model, despite the presence of bounded, nonvanishing disturbances. The
hypersonic vehicle has time varying parameters, specifically temperature profiles, and its
dynamics can be reduced to an LPV system with additive disturbances. Since the HSV
can be modeled as an LPV system the proposed control design is directly applicable. The
control performance is directly examined through simulations.

A wide variety of applications exist that can be effectively modeled as LPV systems.
In particular, flight systems have historically been modeled as LPV systems and associated
control tools have been applied such as gain-scheduling, linear matrix inequalities (LMIs),
linear fractional transformations (LFT), and μ-types. However, as the type of flight
environments and trajectories become more demanding, the traditional LPV controllers
may no longer be sufficient. In particular, hypersonic flight vehicles (HSVs) present an
inherently difficult problem because of the nonlinear aerothermoelastic coupling effects in
the dynamics. HSV flight conditions produce temperature variations that can alter both
the structural dynamics and flight dynamics. Starting with the full nonlinear dynamics,
the aerothermoelastic effects are modeled by a temperature dependent, parameter varying

state-space representation with added disturbances. The model includes an uncertain parameter varying state matrix, an uncertain parameter varying non-square (column deficient) input matrix, and an additive bounded disturbance. In this dissertation, a robust dynamic controller is formulated for a uncertain and disturbed LPV system. The developed controller is then applied to a HSV model, and a Lyapunov analysis is used to prove global exponential reference model tracking in the presence of uncertainty in the state and input matrices and exogenous disturbances. Simulations with a spectrum of gains and temperature profiles on the full nonlinear dynamic model of the HSV is used to illustrate the performance and robustness of the developed controller.

In addition, this work considers how the performance of the developed controller varies over a wide variety of control gains and temperature profiles and are optimized with respect to different performance metrics. Specifically, various temperature profile models and related nonlinear temperature dependent disturbances are used to characterize the relative control performance and effort for each model. Examining such metrics as a function of temperature provides a potential inroad to examine the interplay between structural/thermal protection design and control development and has application for future HSV design and control implementation.

CHAPTER 1
INTRODUCTION

1.1 Motivation and Problem Statement

Recent research on nonlinear inversion of the input dynamics based on Lyapunov stability theory provides a stepping stone to LPV dynamic inversion. In [27, 28], dynamic inversion techniques are used to design controllers that can adaptively and robustly stabilize state-space systems with uncertain constant parameters and additive unknown bounded disturbances. However, this work is limited to time-invarient parameters and therefore is not applicable to LPV systems. The work presented in this chapter is an extension of the work in [27, 28], and provides a continuous robust controller that is able to stabilize general perturbed LPV systems with disturbances, when both the state, input matrices, time-varying parameters, and disturbances are unknown.

The design of guidance and control systems for airbreathing HSV is challenging because the dynamics of the HSV are complex and highly coupled as in [10], and temperature-induced stiffness variations impact the structural dynamics such as in [21]. Much of this difficulty arises from the aerodynamic, thermodynamic, and elastic coupling (aerothermoelasticity) inherent in HSV systems. Because HSV travel at such high velocities (in excess of Mach 5) there are large amounts of aerothermal heating. Aerothermal heating is non-uniform, generally producing much higher temperatures at the stagnation point of airflow near the front of the vehicle. Coupled with additional heating due to the engine, HSVs have large thermal gradients between the nose and tail. The structural dynamics, in turn, affect the aerodynamic properties. Vibration in the forward fuselage changes the apparent turn angle of the flow, which results in changes in the pressure distribution over the forebody of the aircraft. The resulting changes in the pressure distribution over the aircraft manifest themselves as thrust, lift, drag, and pitching moment perturbations as in [10]. To develop control laws for the longitudinal dynamics of a HSV

capable of compensating for these structural and aerothermoelastic effects, structural temperature variations and structural dynamics must be considered.

Aerothermoelasticity is the response of elastic structures to aerodynamic heating and loading. Aerothermoelastic effects cannot be ignored in hypersonic flight, because such effects can destabilize the HSV system as in [21]. A loss of stiffness induced by aerodynamic heating has been shown to potentially induce dynamic instability in supersonic/hypersonic flight speed regimes as in [1]. Yet active control can be used to expand the flutter boundary and convert unstable limit cycle oscillations (LCO) to stable LCO as shown in [1]. An active structural controller was developed in [26], which accounts for variations in the HSV structural properties resulting from aerothermoelastic effects. The control design in [26] models the structural dynamics using a LPV framework, and states the benefits to using the LPV framework are two-fold: the dynamics can be represented as a single model, and controllers can be designed that have affine dependency on the operating parameters.

Previous publications have examined the challenges associated with the control of HSVs. For example, HSV flight controllers are designed using genetic algorithms to search a design parameter space where the nonlinear longitudinal equations of motion contain uncertain parameters as in [4, 30, 49]. Some of these designs utilize Monte Carlo simulations to estimate system robustness at each search iteration. Another approach [4] is to use fuzzy logic to control the attitude of the HSV about a single low end flight condition. While such approaches as in [4, 30, 49] generate stabilizing controllers, the procedures are computationally demanding and require multiple evaluation simulations of the objective function and have large convergent times. An adaptive gain-scheduled controller in [55] was designed using estimates of the scheduled parameters, and a semi-optimal controller is developed to adaptively attain H_∞ control performance. This controller yields uniformly bounded stability due to the effects of approximation errors and algorithmic errors in the neural networks. Feedback linearization techniques have been applied to a control-oriented HSV model to design a nonlinear controller as in [32].

The model in [32] is based on a previously developed HSV longitudinal dynamic model in [8]. The control design in [32] neglects variations in thrust lift parameters, altitude, and dynamic pressure. Linear output feedback tracking control methods have been developed in [44], where sensor placement strategies can be used to increase observability, or reconstruct full state information for a state-feedback controller. A robust output feedback technique is also developed for the linear parameterizable HSV model, which does not rely on state observation. A robust setpoint regulation controller in [17] is designed to yield asymptotic regulation in the presence of parametric and structural uncertainty in a linear parameterizable HSV system.

An adaptive controller in [19] was designed to handle (linear in the parameters) modeling uncertainties, actuator failures, and non-minimum phase dynamics as in [17] for a HSV with elevator and fuel ratio inputs. Another adaptive approach in [41] was recently developed with the addition of a guidance law that maintains the fuel ratio within its choking limits. While adaptive control and guidance control strategies for a HSV are investigated in [17, 19, 41], neither addresses the case where dynamics include unknown and unmodeled disturbances. There remains a need for a continuous controller, which is capable of achieving exponential tracking for a HSV dynamic model containing aerothermoelastic effects and unmodeled disturbances (i.e., nonvanishing disturbances that do not satisfy the linear in the parameters assumption).

In the context of the aforementioned literature, a contribution of this dissertation (and in the publications in [51] and [52]) is the development of a controller that achieves exponential model reference output tracking despite an uncertain model of the HSV that includes nonvanishing exogenous disturbances. A nonlinear temperature-dependent parameter-varying state-space representation is used to capture the aerothermoelastic effects and unmodeled uncertainties in a HSV. This model includes an unknown parameter-varying state matrix, an uncertain parameter-varying non-square (column deficient) input matrix, and a nonlinear additive bounded disturbance. To achieve an exponential tracking

result in light of these disturbances, a robust, continuous Lyapunov-based controller is developed that includes a novel implicit learning characteristic that compensates for the nonvanishing exogenous disturbance. That is, the use of the implicit learning method enables the first exponential tracking result by a continuous controller in the presence of the bounded nonvanishing exogenous disturbance. To illustrate the performance of the developed controller, simulations are performed on the full nonlinear model given in [10] that includes aerothermoelastic model uncertainties and nonlinear exogenous disturbances whose magnitude is based on airspeed fluctuations.

In addition to the control development, there exists the need to understand the interplay of a control design with respect to the vehicle dynamics. A previous control oriented design analysis in [6] states that simultaneously optimizing both the structural dynamics and control is an intractable problem, but that control-oriented design may be performed by considering the closed-loop performance of an optimal controller on a series of different open-loop design models. The best performing design model is then said to have the optimal dynamics in the sense of controllability. Knowledge of the optimal thermal gradients will provide insight to engineers on how to properly weight the HSV's thermal protection system for both steady-state and transient flight. The preliminary work by authors in [6] provides a control-oriented design architecture by investigating control performance variations due to thermal gradients using an $\mathcal{H}_\infty$ controller. Chapter 5 seeks to extend the control oriented design concept to examine control performance variations for HSV models that include nonlinear aerothermoelastic disturbances. Given these disturbances, Chapter 5 focuses on examining control performance variations for the model reference robust controller in Chapter 2 and Chapter 4 to achieve a nonlinear control-oriented analysis with respect to thermal gradients on the HSV. By analyzing control error and input norms as well as transient and steady-state responses over a wide range of temperature profiles an optimal temperature profile range is suggested.

1.2   Outline and Contributions

This dissertation focuses on designing a nonlinear controller for general disturbed LPV system. The controller is then modified for a specific air-breathing HSV. The dynamic inversion design is a technique that allows the multiplicative input matrices to be inverted, thus rendering the controller affine in the control. Previous results in [27] and [29] have examined full state and output feedback adaptive dynamic inversion controllers, but are limited because they contain constant uncertainties. The HSV system presents a new challenge because the uncertain state and input matrices are parameter varying. Specifically, the state and input matrices of the hypersonic vehicle vary as a function of temperature. This chapter provides some background and motivates the robust dynamic inversion control method subsequently developed. A brief outline of the following chapters follows.

In Chapter 2 a tracking controller is presented that achieves exponential stability of a model reference system in the presence of uncertainties and disturbances. Specifically, the plant model contains time-varying parametric uncertainty with disturbances that are bounded and nonvanishing. The contribution of this result is that it represents the first ever development of an exponentially stable continuous robust model reference tracking controller for an LPV system with an unknown system matrix and uncertain input matrix with an additive unknown bounded disturbance. Lyapunov based methods are used to prove exponential stability of the system.

Chapter 3 provides the nonlinear dynamics and temperature model of a HSV. The nonlinear and highly coupled dynamic equations are presented. The equations that define the aerodynamic and generalized moments and forces are provided explicitly in previous literature. This chapter is meant to serve as an overview of the dynamics of the HSV. In addition to the flight and structural dynamics, temperature profile modeling is provided. Temperature variations impact the HSV flight dynamics through changes in the structural dynamics which affect the mode shapes and natural frequencies of the vehicle.

The presented model offers an approximate approach, whereby the natural frequencies of a continuous beam are described as a function of the mass distribution of a beam and its stiffness. Figures and tables are presented to emphasize the need to include such dynamics for control design. This chapter is designed to familiarize the reader with the HSV dynamic and temperature models, since these dynamics are used throughout this dissertation. This chapter is a precursor and introduction to Chapter 4 and Chapter 5.

Using the controller developed in Chapter 2, the contribution in Chapter 4 is to illustrate an application to an air-breathing hypersonic vehicle system with additive bounded disturbances and aerothermoelastic effects, where the control input is multiplied by an uncertain, column deficient, parameter-varying matrix. In addition to the stability proof, the control design is also validated through implementation in a full nonlinear dynamic simulation. The exogenous disturbances (e.g., wind gust, engine variations, etc.) and temperature profiles (aerodynamic driven thermal heating) are designed to examine the robustness of the developed controller. The results from the simulation illustrate the boundedness of the controller with favorable transient and steady state tracking errors and provide evidence that the control model used for development is valid.

The contribution in Chapter 5 is to provide an analysis framework to examine the nonlinear control performance based on variations in the vehicle dynamics. Specifically, the changes occur in the structural dynamics via their response to different temperature profiles, and hence the observed vibration has different frequencies and shapes. Using an initial random search and evolving algorithms, approximate optimal gains are found for the controller for each temperature dependant plant model. Errors, control effort, transient and steady-state performance analysis is provided. The results from this analysis show that there is a temperature range for operation of the HSV that minimizes a given cost of performance versus control authority. Knowledge of a favorable range with regard to control performance provides designers an extra tool when developing the thermal protection system as well as the structural characteristics of the HSV.

Chapter 6 summarizes the contributions of the dissertation and possible avenues for future work are provided. The brief contributions of the LPV controller, HSV example controller design application, and the HSV optimization procedure provide the base of this dissertation. After a brief summary, some of the drawbacks of the current control design are presented as directions for future research work.

CHAPTER 2
LYAPUNOV-BASED EXPONENTIAL TRACKING CONTROL OF LPV SYSTEMS WITH AN UNKNOWN SYSTEM MATRIX, UNCERTAIN INPUT MATRIX VIA DYNAMIC INVERSION

2.1   Introduction

Linear parameter varying (LPV) systems have a wide range of practical engineering applications. Some examples include several missile autopilot designs as in [7, 39, 43], a turbofan engine [5], and active suspension design [18]. Traditionally, LPV systems have been developed using a gain scheduling control approach. Gain scheduling is a technique to develop controllers for nonlinear system using traditional linear control theory. Gain scheduling is a technique where the system is linearized about certain operating conditions. About these operating conditions, constant parameters are assumed and separate control schemes and gains are chosen. More than a decade ago, Shamma et. al. pointed out some of the potential hazards of gain scheduling in [42]. In particular, gain scheduling is a analytically non-continuous method and stability is not guaranteed while switching from one region of linearization to another. In fact the two biggest downfalls of gain scheduling control design is the linearization of the plant models close to equilibrium or constant parameters states and the requirement that the parameters must change slowly. Because the linearization is required to be close to some operation condition or stability point, many different schedules have to be taken. And by requiring that parameters change slowly, the gain scheduling techniques are not appropriate for many quickly varying systems.

Another approach to LPV problems is the use of linear matrix inequalities (LMIs). In a book on LMIs and their use in system and control theory in [11], Boyd et. al. states that LMIs are mathematically convex optimization problems with extensions to control theory. However in [11] it is pointed out that these typically require numerical solutions and there are only a few special cases where analytical solutions exist. These LPV solutions typically only provide norm based solutions. The most common of these is the

L_2-norm because it allows for continuity with H_∞ control when the systems become linear time-invariant. For instance H_∞ control is developed in [14] which uses LMIs to optimize the solution and in [3], the parameterization of LMIs was investigated in the context of control theory. H_∞ control is developed in [14], which uses LMIs to optimize the solution and Saif et. al. in [48] shows that stabilization solutions exist for multi-input-multi-output (MIMO) systems using LMIs. These designs allow for the continuous solution of LPV systems, however knowledge of the structure of the system must be known, and the parameters are assumed measurable online. In [25] minimax controllers are designed to handle only constant or small variations in the parameters, where the parameterized algebraic Riccati inequalities are converted into equivalent LMIs so that the convexity can be exploited and a controller developed. Continuous control design for uncertain LPV systems in [13] is designed using LMIs, however the procedure is limited to uncertainties in the state matrix, and does not cover uncertainties in the input matrix.

Another approach uses linear fractional transformations LFTs in the context of LPV control design such as in [31] and are based on small gain theory. This approach cannot handle uncertain parameters. However, by extending the solution in [31] the design can include uncertain parameters which are not available to the controller. These solutions are μ-synthesis type controllers, however the solvability conditions are non-convex and therefore a solution to the problem is not guaranteed even when a stable controller exists. Several examples of recursive μ-type solutions are given in [2, 22, 45]. More recently in [26], the μ-type solutions have been extended to a hypersonic aircraft example, but suffers the same non-convexity problem as the formerly listed μ-type literature.

Recent research on nonlinear inversion of the input dynamics based on Lyapunov stability theory provides a stepping stone to LPV dynamic inversion. In [27, 28], dynamic inversion techniques are used to design controllers that can adaptively and robustly stabilize a more general state-space system that has been considered in previous work with uncertain constant parameters and additive unknown bounded disturbances. However,

this work is limited to time-invarient parameters and therefore is not applicable to LPV systems. The work presented in this chapter is an extension of the work in [27, 28], and provides a continuous robust controller that is able to exponentially stabilize LPV systems with unknown bounded disturbances, when both the state, input matrices, time-varying parameters, and disturbances are unknown.

2.2 Linear Parameter Varying Model

The dynamic model used for the subsequent control development is a combination of linear-parameter-varying (LPV) system with an added unmodeled disturbance as

$$\dot{x} = A\left(\rho\left(t\right)\right)x + B\left(\rho\left(t\right)\right)u + f\left(t\right) \tag{2–1}$$

$$y = Cx. \tag{2–2}$$

In (2–1) and (2–2), $x\left(t\right) \in \mathbb{R}^n$ is the state vector, $A\left(\rho\left(t\right)\right) \in \mathbb{R}^{n \times n}$ denotes a linear parameter varying state matrix, $B\left(\rho\left(t\right)\right) \in R^{n \times p}$ denotes a linear parameter varying input matrix, $C \in \mathbb{R}^{q \times n}$ denotes a known output matrix, $u(t) \in \mathbb{R}^p$ denotes control vector, $\rho\left(t\right)$ represents the unknown time-dependent parameters, $f(t) \in \mathbb{R}^n$ represents a time-dependent unknown, nonlinear disturbance, and $y\left(t\right) \in \mathbb{R}^q$ represents the measured output vector. The subsequent control development is based on the assumption that $p \geq q$, meaning that at least one control input is available for each output state. When the system is overactuated in that there are more control inputs available than output states, then $p > q$ and the resulting input dynamic inversion matrix will be row deficient. For this case, a right pseudo-inverse can be used in conjunction with a singularity avoidance law. For instance, if $\sigma \in \mathbb{R}^{q \times p}$ then the pseudo-inverse $\sigma^+ = \sigma^T \left(\sigma\sigma^T\right)^{-1}$ and satisfies $\sigma\sigma^+ = I_{q \times q}$ where $I_{q \times q}$ is an identity matrix of dimension $q \times q$.

The matrices $A\left(\rho\left(t\right)\right)$ and $B\left(\rho\left(t\right)\right)$ have the standard linear parameter-varying form

$$A\left(\rho, t\right) = A_0 + \sum_{i=1}^{s} w_i\left(\rho\left(t\right)\right) A_i \tag{2–3}$$

$$B\left(\rho, t\right) = B_0 + \sum_{i=1}^{s} v_i\left(\rho\left(t\right)\right) B_i \tag{2–4}$$

where $A_0 \in \mathbb{R}^{n \times n}$ and $B_0 \in \mathbb{R}^{n \times p}$ represent known nominal matrices with unknown variations $w_i \left(\rho \left(t \right) \right) A_i$ and $v_i \left(\rho \left(t \right) \right) B_i$ for $i = 1, 2, ..., s$, where $A_i \in \mathbb{R}^{n \times n}$ and $B_i \in \mathbb{R}^{n \times p}$ are time-invariant matrices, and $w_i \left(\rho \left(t \right) \right), v_i \left(\rho \left(t \right) \right) \in \mathbb{R}$ are parameter-dependent weighting terms. Knowledge of the nominal matrix B_0 will be exploited in the subsequent control design.

To facilitate the subsequent control design, a reference model is given as

$$\dot{x}_m = A_m x_m + B_m \delta \tag{2–5}$$

$$y_m = C x_m \tag{2–6}$$

where $A_m \in \mathbb{R}^{n \times n}$ and $B_m \in \mathbb{R}^{n \times p}$ denote the state and input matrices, respectively, where A_m is Hurwitz, $\delta \left(t \right) \in \mathbb{R}^p$ is a vector of reference inputs, $y_m \left(t \right) \in \mathbb{R}^q$ are the reference outputs, and C was defined in (2–2).

Assumption 1: The nonlinear disturbance $f \left(t \right)$ and its first two time derivatives are assumed to exist and be bounded by known constants.

Assumption 2: The dynamics in (2–1) are assumed to be controllable.

Assumption 3: The matrices $A \left(\rho \left(t \right) \right)$ and $B \left(\rho \left(t \right) \right)$ and their time derivatives satisfy the following inequalities:

$$\| A \left(\rho \left(t \right) \right) \|_\infty \leq \zeta_A \qquad \| B \left(\rho \left(t \right) \right) \|_\infty \leq \zeta_B \tag{2–7}$$

$$\left\| \dot{A} \left(\rho \left(t \right) \right) \right\|_\infty \leq \zeta_{Ad} \qquad \left\| \dot{B} \left(\rho \left(t \right) \right) \right\|_\infty \leq \zeta_{Bd}$$

where $\zeta_A, \zeta_B, \zeta_{Ad}, \zeta_{Bd} \in \mathbb{R}^+$ are known bounding constants, and $\| \cdot \|_\infty$ denotes the induced infinity norm of a matrix. As is typical in robust control methods, knowledge of the upper bounds in (2–7) are used to develop sufficient conditions on gains used in the subsequent control design.

2.3 Control Development

2.3.1 Control Objective

The control objective is to ensure that the output $y(t)$ tracks the time-varying output generated from the reference model in (2–5) and (2–6). To quantify the control objective, an output tracking error, denoted by $e(t) \in \mathbb{R}^q$, is defined as

$$e \triangleq y - y_m = C(x - x_m). \tag{2–8}$$

To facilitate the subsequent analysis, a filtered tracking error denoted by $r(t) \in \mathbb{R}^q$, is defined as

$$r \triangleq \dot{e} + \gamma e \tag{2–9}$$

where $\gamma \in \mathbb{R}^2$ is a positive definite diagonal, constant control gain matrix, and is selected to place a relative weight on the error state verses its derivative. To facilitate the subsequent robust control development, the state vector $x(t)$ is expressed as

$$x(t) = \underline{x}(t) + x_u(t) \tag{2–10}$$

where $\underline{x}(t) \in \mathbb{R}^n$ contains the p output states, and $x_u(t) \in \mathbb{R}^n$ contains the remaining $n - p$ states. Likewise, the reference states $x_m(t)$ can also be separated as in (2–10).

Assumption 4: The states contained in $x_u(t)$ in (2–10) and the corresponding time derivatives can be further separated as

$$x_u(t) = x_{\rho u}(t) + x_{\zeta u}(t) \tag{2–11}$$

$$\dot{x}_u(t) = \dot{x}_{\rho u}(t) + \dot{x}_{\zeta u}(t)$$

where $x_{\rho u}(t), \dot{x}_{\rho u}(t), x_{\zeta u}(t), \dot{x}_{\zeta u}(t) \in \mathbb{R}^n$ are upper bounded as

$$\|x_{\rho u}(t)\| \le c_1 \|z\| \qquad \|x_{\zeta u}(t)\| \le \zeta_{xu} \tag{2–12}$$

$$\|\dot{x}_{\rho u}(t)\| \le c_2 \|z\| \qquad \|\dot{x}_{\zeta u}(t)\| \le \zeta_{\dot{x}u}$$

where $z(t) \in \mathbb{R}^{2q}$ is defined as

$$z \triangleq \begin{bmatrix} e^T & r^T \end{bmatrix}^T \tag{2–13}$$

and $c_1, c_2, \zeta_{xu}, \zeta_{\dot{x}u} \in \mathbb{R}$ are known non-negative bounding constants. The terms in (2–11) and (2–12) are used to develop sufficient gain conditions for the subsequent robust control design.

2.3.2 Open-Loop Error System

The open-loop tracking error dynamics can be developed by taking the time derivative of (2–9) and using the expressions in (2–1)-(2–6) as

$$\dot{r} = \ddot{e} + \gamma \dot{e}$$

$$= C \left(\ddot{x} - \ddot{x}_m \right) + \gamma \dot{e}$$

$$= C \left(\dot{A}x + A\dot{x} + \dot{B}u + B\dot{u} + \dot{f}(t) - A_m \dot{x}_m - B_m \dot{\delta} \right) + \gamma \dot{e}$$

$$= \tilde{N} + N_d + C\dot{B}u + CB\dot{u} - e. \tag{2–14}$$

The auxiliary functions $\tilde{N}\left(x, \dot{x}, e, x_m, \dot{x}_m, t\right) \in \mathbb{R}^q$ and $N_d\left(x_m, \dot{x}_m, \delta, \dot{\delta}, t\right) \in \mathbb{R}^q$ in (2–14) are defined as

$$\tilde{N} \triangleq CA\left(\underline{\dot{x}} - \underline{\dot{x}}_m\right) + C\dot{A}\left(\underline{x} - \underline{x}_m\right) + CA\dot{x}_{\rho u} + C\dot{A}x_{\rho u} + \gamma \dot{e} + e \tag{2–15}$$

and

$$N_d \triangleq C\dot{f}(t) + CA\dot{x}_{\zeta u} + C\dot{A}x_{\zeta u} + CA\underline{\dot{x}}_m + C\dot{A}\underline{x}_m - CA_m \dot{x}_m - CB_m \dot{\delta}. \tag{2–16}$$

Motivation for the selective grouping of the terms in (2–15) and (2–16) is derived from the fact that the following inequalities can be developed [38, 54] as

$$\left\| \tilde{N} \right\| \leq \rho_0 \left\| z \right\| \qquad \left\| N_d \right\| \leq \zeta_{N_d}, \tag{2–17}$$

where $\rho_0, \zeta_{N_d} \in \mathbb{R}^+$ are known bounding constants.

2.3.3 Closed-Loop Error System

Based on the expression in (2–14) and the subsequent stability analysis, the control input is designed as

$$u = -k_\Gamma \left(CB_0\right)^{-1} \left[\left(k_s + I_{q\times q}\right) e\left(t\right) - \left(k_s + I_{q\times q}\right) e\left(0\right) + \upsilon\left(t\right)\right] \tag{2–18}$$

where $\upsilon\left(t\right) \in \mathbb{R}^q$ is an implicit learning law with an update rule given by

$$\dot{\upsilon}\left(t\right) = k_u \left\|u\left(t\right)\right\| sgn\left(r\left(t\right)\right) + \left(k_s + I_{q\times q}\right) \gamma e\left(t\right) + k_\gamma sgn\left(r\left(t\right)\right) \tag{2–19}$$

and $k_\Gamma \in \mathbb{R}^{p\times p}$, $k_u, k_s, k_\gamma \in \mathbb{R}^{q\times q}$ denote positive definite, diagonal constant control gain matrices, $B_0 \in \mathbb{R}^{n\times p}$ is introduced in (2–4), $sgn\left(\cdot\right)$ denotes the standard signum function where the function is applied to each element of the vector argument, and $I_{q\times q}$ denotes a $q \times q$ identity matrix.

After substituting the time derivative of (2–18) into (2–14), the error dynamics can be expressed as

$$\dot{r} = \tilde{N} + N_d - \tilde{\Omega} k_u \left\|u\left(t\right)\right\| sgn\left(r\left(t\right)\right) + CB\dot{u} \tag{2–20}$$

$$- \tilde{\Omega} \left(k_s + I_{p\times p}\right) r\left(t\right) - \tilde{\Omega} k_\gamma sgn\left(r\left(t\right)\right) - e$$

where the auxiliary matrix $\tilde{\Omega}\left(\rho\left(t\right)\right) \in \mathbb{R}^{q\times q}$ is defined as

$$\tilde{\Omega} \triangleq CBk_\Gamma \left(CB_0\right)^{-1} \tag{2–21}$$

where $\tilde{\Omega}\left(\rho\left(t\right)\right)$ can be separated into diagonal (i.e., $\Lambda\left(\rho\left(t\right)\right) \in \mathbb{R}^{q\times q}$) and off-diagonal (i.e., $\Delta\left(\rho\left(t\right)\right) \in \mathbb{R}^{q\times q}$) components as

$$\tilde{\Omega} = \Lambda + \Delta. \tag{2–22}$$

Assumption 5: The subsequent development is based on the assumption that the uncertain matrix $\tilde{\Omega}\left(\rho\left(t\right)\right)$ is diagonally dominant in the sense that

$$\lambda_{\min}\left(\Lambda\right) - \left\|\Delta\right\|_{i\infty} > \varepsilon \tag{2–23}$$

25

where $\varepsilon \in \mathbb{R}^+$ is a known constant. While this assumption cannot be validated for a generic system, the condition can be checked (within some certainty tolerances) for a specific system. Essentially, this condition indicates that the nominal value B_0 must remain within some bounded region of B. In practice, bounds on the variation of B should be known, for a particular system under a set of operating conditions, and this bound can be used to check the sufficient conditions given in (2–23).

Motivation for the structure of the controller in (2–18) and (2–19) comes from the desire to develop a closed-loop error system to facilitate the subsequent Lyapunov-based stability analysis. In particular, since the control input is premultiplied by the uncertain matrix CB in (2–14), the term CB_0^{-1} is motivated to generate the relationship in (2–21) so that if the diagonal dominance assumption (Assumption 5) is satisfied, then the control can provide feedback to compensate for the disturbance terms. The bracketed terms in (2–18) include the state feedback, an initial condition term, and the implicit learning term. The implicit learning term $\upsilon(t)$ is the generalized solution to (2–19). The structure of the update law in (2–19) is motivated by the need to reject the exogenous disturbance terms. Specifically, the update law is motivated by a sliding mode control strategy that can be used to eliminate additive bounded disturbances. Unlike sliding mode control (which is a discontinuous control method requiring infinite actuator bandwidth), the current continuous control approach includes the integral of the $sgn(\cdot)$ function. This implicit learning law is the key element that allows the controller to obtain an exponential stability result despite the additive nonvanishing exogenous disturbance. Other results in literature also have used the implicit learning structure include [33, 34, 35, 36, 37, 40].

Differential equations such as (2–24) and (2–25) have discontinuous right-hand sides as

$$\dot{\upsilon}(t) = k_u \|u(t)\|\, sgn(r(t)) + (k_s + I_{p\times p})\gamma e(t) + k_\gamma sgn(r(t)) \tag{2–24}$$

$$\dot{r} = \tilde{N} + N_d - \tilde{\Omega}k_u \|u(t)\|\, sgn(r(t)) + C\dot{B}u - \tilde{\Omega}(k_s + I_{p\times p})r(t) - \tilde{\Omega}k_\gamma sgn(r(t)) - e. \tag{2–25}$$

Let $f_{fil}(y,t) \in \mathbb{R}^{2p}$ denote the right-hand side of (2–24) and (2–25). Since the subsequent analysis requires that a solution exist for $\dot{y} = f_{fil}(y,t)$, it is important to show the existence of the generalized solution. The existence of Filippov's generalized solution [15] can be established for (2–24) and (2–25). First, note that $f_{fil}(y,t)$ is continuous except in the set $\{(y,t)\,|\,r=0\}$. Let $F(y,t)$ be a compact, convex, upper semicontinuous set-valued map that embeds the differential equation $\dot{y} = f_{fil}(x,t)$ into the differential inclusion $\dot{y} \in F(y,t)$. An absolute continuous solution exists to $\dot{y} = F(x,t)$ that is a generalized solution to $\dot{y} = f_{fil}(x,t)$. A common choice [15] for $F(y,t)$ that satisfies the above conditions is the closed convex hull of $f_{fil}(y,t)$. A proof that this choice for $F(y,t)$ is upper semicontinuous is given in [20].

2.4 Stability Analysis

Theorem: The controller given in (2–18) and (2–19) ensures exponential tracking in the sense that

$$\|e(t)\| \le \|z(0)\| \exp\left(-\frac{\lambda_1}{2}t\right) \qquad \forall t \in [0,\infty), \tag{2–26}$$

where $\lambda_1 \in \mathbb{R}^+$, provided the control gains k_u, k_s, and k_γ introduced in (2–18) are selected according to the sufficient conditions

$$\lambda_{\min}(k_u) \ge \frac{\bar{\zeta}_{Bd}}{\varepsilon} \qquad \lambda_{\min}(k_s) > \frac{\rho_0^2}{4\varepsilon\min\{\gamma,\varepsilon\}} \qquad \lambda_{\min}(k_\gamma) > \frac{\zeta_{N_d}}{\varepsilon}, \tag{2–27}$$

where ρ_0 and ζ_{N_d} are introduced in (2–17), ε is introduced in (2–23), $\bar{\zeta}_{Bd} \in \mathbb{R}^+$ is a known positive constant, and $\lambda_{\min}(\cdot)$ denotes the minimum eigenvalue of the argument. The bounding constants are conservative upper bounds on the maximum expected

values. The Lyapunov analysis indicates that the gains in (2–27) need to be selected sufficiently large based on the bounds. Therefore, if the constants are chosen to be conservative, then the sufficient gain conditions will be larger. Values for these gains could be determined through a physical understanding of the system (within some conservative % of uncertainty) and/or through numerical simulations.

Proof: Let $V_L(z,t) : \mathbb{R}^{2q} \times [0,\infty) \to \mathbb{R}$ be a Lipschitz continuous, positive definite function defined as

$$V_L(z,t) \triangleq \frac{1}{2}e^T e + \frac{1}{2}r^T r \tag{2–28}$$

where $e(t)$ and $r(t)$ are defined in (2–8) and (2–9), respectively. After taking the time derivative of (2–28) and utilizing (2–9), (2–20), and (2–22), $\dot{V}_L(z,t)$ can be expressed as

$$\dot{V}_L(z,t) = -\gamma e^T e + r^T \tilde{N} + r^T C \dot{B} u - r^T \Lambda (k_s + I_{p\times p}) r - r^T \Delta (k_s + I_{p\times p}) r \tag{2–29}$$
$$- r^T \Lambda \|u\| k_u sgn(r) - r^T \Delta \|u\| k_u sgn(r) - r^T \Lambda k_\gamma sgn(r)$$
$$- r^T \Delta k_\gamma sgn(r) + r^T N_d.$$

By utilizing the bounding arguments in (2–17) and Assumptions 3 and 5, the upper bound of the expression in (2–29) can be explicitly determined. Specifically, based on (2–7) of Assumption 3, the term $r^T C \dot{B} u$ in (2–29) can be upper bounded as

$$r^T C \dot{B} u \leq \bar{\zeta}_{Bd} \|r\| \|u\|. \tag{2–30}$$

After utilizing inequality (2–23) of Assumption 5, the following inequalities can be developed:

$$-r^T \Lambda (k_s + I_{p\times p}) r - r^T \Delta (k_s + I_{p\times p}) r \leq -\varepsilon (\lambda_{\min}(k_s) + 1) \|r\|^2$$
$$-r^T \Lambda \|u(t)\| k_u sgn(r) - r^T \Delta \|u(t)\| k_u sgn(r) \leq -\varepsilon \lambda_{\min}(k_u) |r| \|u\| \tag{2–31}$$
$$-r^T \Lambda k_\gamma sgn(r) - r^T \Delta k_\gamma sgn(r) \leq -\varepsilon \lambda_{\min}(k_\gamma) |r|.$$

After using the inequalities in (2–30) and (2–31), the expression in (2–29) can be upper bounded as

$$\dot{V}_L(z,t) \le -\gamma \|e\|^2 + r^T \tilde{N} + \bar{\zeta}_{Bd} \|r\| \|u\| - \varepsilon (\lambda_{\min}(k_s) + 1) \|r\|^2 \tag{2–32}$$
$$- \varepsilon \lambda_{\min}(k_u) \|r\| \|u\| - \varepsilon \lambda_{\min}(k_\gamma) \|r\| + r^T N_d,$$

where the fact that $|r| \ge \|r\| \ \forall \ r \in \mathbb{R}^q$ was utilized. After utilizing the inequalities in (2–17) and rearranging the resulting expression, the upper bound for $\dot{V}_L(z,t)$ can be expressed as

$$\dot{V}_L(z,t) \le -\gamma \|e\|^2 - \varepsilon \|r\|^2 - \varepsilon \lambda_{\min}(k_s) \|r\|^2 + \rho_0 \|r\| \|z\| \tag{2–33}$$
$$- [\varepsilon \lambda_{\min}(k_u) - \zeta_{Bd}] \|r\| \|u\| - [\varepsilon \lambda_{\min}(k_\gamma) - \zeta_{N_d}] \|r\|.$$

If k_u and k_γ satisfy the sufficient gain conditions in (2–27), the bracketed terms in (2–33) are positive, and $\dot{V}_L(z,t)$ can be upper bounded using the squares of the components of $z(t)$ as:

$$\dot{V}_L(z,t) \le -\gamma \|e\|^2 - \varepsilon \|r\|^2 - \left[\varepsilon \lambda_{\min}(k_s) \|r\|^2 - \rho_0 \|r\| \|z\| \right]. \tag{2–34}$$

By completing the squares, the upper bound in (2–34) can be expressed in a more convenient form. To this end, the term $\frac{\rho_0^2 \|z\|^2}{4\varepsilon \lambda_{\min}(k_s)}$ is added and subtracted to the right hand side of (2–34) yielding

$$\dot{V}_L(z,t) \le -\gamma \|e\|^2 - \varepsilon \|r\|^2 - \varepsilon \lambda_{\min}(k_s) \left[\|r\| - \frac{\rho_0 \|z\|}{2\varepsilon \lambda_{\min}(k_s)} \right]^2 + \frac{\rho_0^2 \|z\|^2}{4\varepsilon \lambda_{\min}(k_s)}. \tag{2–35}$$

Since the square of the bracketed term in (2–35) is always positive, the upper bound can be expressed as

$$\dot{V}_L(z,t) \le -z^T diag \{\gamma I_{p \times p}, \varepsilon I_{p \times p}\} z + \frac{\rho_0^2 \|z\|^2}{4\varepsilon \lambda_{\min}(k_s)}, \tag{2–36}$$

where $z(t)$ is defined in (2–13). Hence, (2–36) can be used to rewrite the upper bound of $\dot{V}_L(z,t)$ as

$$\dot{V}_L(z,t) \le -\left(\min\{\gamma, \varepsilon\} - \frac{\rho_0^2}{4\varepsilon \lambda_{\min}(k_s)} \right) \|z\|^2, \tag{2–37}$$

where the fact that $z^T diag \{\gamma I_{p \times p}, \varepsilon I_{p \times p}\} z \geq \min \{\gamma, \varepsilon\} \|z\|^2$ was utilized. Provided the gain condition in (2–27) is satisfied, (2–28) and (2–37) can be used to show that $V_L(t) \in L_\infty$; hence $e(t), r(t) \in L_\infty$. Given that $e(t), r(t) \in L_\infty$, standard linear analysis methods can be used to prove that $\dot{e}(t) \in L_\infty$ from (2–9). Since $e(t), \dot{e}(t) \in L_\infty$, the assumption that the reference model outputs $y_m(t), \dot{y}_m(t) \in L_\infty$ can be used along with (2–8) to prove that $y(t), \dot{y}(t) \in L_\infty$. Given that $y(t), \dot{y}(t), e(t), r(t) \in L_\infty$, the vector $\underline{x}(t) \in L_\infty$, the time derivative $\underline{\dot{x}}(t) \in L_\infty$, and (2–10)-(2–12) can be used to show that $x(t), \dot{x}(t) \in L_\infty$. Given that $x(t), \dot{x}(t) \in L_\infty$, Assumptions 1, 2, and 3 can be utilized along with (2–1) to show that $u(t) \in L_\infty$.

The definition for $V_L(z, t)$ in (2–28) can be used along with inequality (2–37) to show that $V_L(z, t)$ can be upper bounded as

$$\dot{V}_L(z, t) \leq -\lambda_1 V_L(z, t) \tag{2–38}$$

provided the sufficient condition in (2–27) is satisfied. The differential inequality in (2–38) can be solved as

$$V_L(z, t) \leq V_L(z(0), 0) \exp(-\lambda_1 t). \tag{2–39}$$

Hence, (2–13), (2–28), and (2–39) can be used to conclude that

$$\|e(t)\| \leq \|z(0)\| \exp\left(-\frac{\lambda_1}{2}t\right) \qquad \forall t \in [0, \infty). \tag{2–40}$$

2.5 Conclusions

A continuous exponentially stable controller was developed for LPV systems with an unknown state matrix, an uncertain input matrix, and an unknown additive disturbance. This work presents a new approach to LPV control by inverting the uncertain input dynamics and robustly compensating for other unknowns and disturbances. The controller is valid for LPV systems where there are at least as many control inputs as there are outputs. Using this technique it is possible control LPV systems where there is a high amount of uncertainty and nonlinearities that invalidate traditional LPV approaches.

Robust dynamic inversion control is possible for a wide range of practical systems that are approximated as an LPV system with additive disturbances. Future work will focus on relaxing the assumptions while maintaining the stability and performance.

CHAPTER 3
HYPERSONIC VEHICLE DYNAMICS AND TEMPERATURE MODEL

3.1 Introduction

In this chapter the dynamics of the hypersonic vehicle (HSV) are introduced, including both the standard flight dynamics and the structural vibration dynamics. After the dynamics are developed and the flight and structural components are explained, a temperature model is introduced. Because changes in temperature change the structural dynamics, coupled forcing terms change the the flight dynamics. Examples of linear temperature profiles are provided, and some examples of the structural modes and frequencies are explained.

3.2 Rigid Body and Elastic Dynamics

To incorporate structural dynamics and aerothermoelastic effects in the HSV dynamic model, an assumed modes model is considered for the longitudinal dynamics [53] as

$$\dot{V} = \frac{T \cos{(\alpha)} - D}{m} - g \sin{(\theta - \alpha)} \tag{3-1}$$

$$\dot{h} = V \sin{(\theta - \alpha)} \tag{3-2}$$

$$\dot{\alpha} = -\frac{L + T \sin{(\alpha)}}{mV} + Q + \frac{g}{V} \cos{(\theta - \alpha)} \tag{3-3}$$

$$\dot{\theta} = Q \tag{3-4}$$

$$\dot{Q} = \frac{M}{I_{yy}} \tag{3-5}$$

$$\ddot{\eta}_i = -2\zeta_i \omega_i \dot{\eta}_i - \omega_i^2 \eta_i + N_i, \qquad i = 1, 2, 3. \tag{3-6}$$

In (3–1)-(3–6), $V(t) \in R$ denotes the forward velocity, $h(t) \in R$ denotes the altitude, $\alpha(t) \in R$ denotes the angle of attack, $\theta(t) \in R$ denotes the pitch angle, $Q(t) \in R$ is pitch rate, and $\eta_i(t) \in R \ \forall i = 1, 2, 3$ denotes the ith generalized structural mode displacement. Also in (3–1)-(3–6), $m \in R$ denotes the vehicle mass, $I_{yy} \in R$ is the moment of inertia, $g \in R$ is the acceleration due to gravity, $\zeta_i(t), \omega_i(t) \in R$ are the damping factor and natural frequency of the ith flexible mode, respectively, $T(x) \in R$ denotes the thrust,

$D(x) \in R$ denotes the drag, $L(x) \in R$ is the lift, $M(x) \in R$ is the pitching moment about the body y-axis, and $N_i(x) \in R \; \forall i = 1, 2, 3$ denotes the generalized elastic forces, where $x(t) \in R^{11}$ is composed of the 5 flight and 6 structural dynamic states as

$$x = \begin{bmatrix} V & \alpha & Q & h & \theta & \eta_1 & \dot{\eta}_1 & \eta_2 & \dot{\eta}_2 & \eta_3 & \dot{\eta}_3 \end{bmatrix}^T. \tag{3-7}$$

The equations that define the aerodynamic and generalized moments and forces are highly coupled and are provided explicitly in previous work [10]. Specifically, the rigid body and elastic modes are coupled in the sense that $T(x)$, $D(x)$, $L(x)$, are functions of $\eta_i(t)$ and that $N_i(x)$ is a function of the other states. As the temperature profile changes, the modulus of elasticity of the vehicle changes and the damping factors and natural frequencies of the flexible modes will change. The subsequent development exploits an implicit learning control structure, designed based on an LPV approximation of the dynamics in (3–1)-(3–6), to yield exponential tracking despite the uncertainty due to the unknown aerothermoelastic effects and additional unmodeled dynamics.

3.3   Temperature Profile Model

Temperature variations impact the HSV flight dynamics through changes in the structural dynamics which affect the mode shapes and natural frequencies of the vehicle. The temperature model used assumes a free-free beam [10], which may not capture the actual aircraft dynamics properly. In reality, the internal structure will be made of a complex network of structural elements that will expand at different rates causing thermal stresses. Thermal stresses affect different modes in different manners, where it raises the frequencies of some modes and lowers others (compared to a uniform degradation with Young's modulus only). Therefore, the current model only offers an approximate approach. The natural frequencies of a continuous beam are a function of the mass distribution of the beam and the stiffness. In turn, the stiffness is a function of Young's Modulus (E) and admissible mode functions. Hence, by modeling Young's Modulus as a function of temperature, the effect of temperature on flight dynamics can be captured.

Thermostructural dynamics are calculated under the material assumption that titanium is below the thermal protection system [9, 12]. Young's Modulus (E) and the natural dynamic frequencies for the first three modes of a titanium free-free beam are depicted in Figure 3-1 and Figure 3-2 respectively.
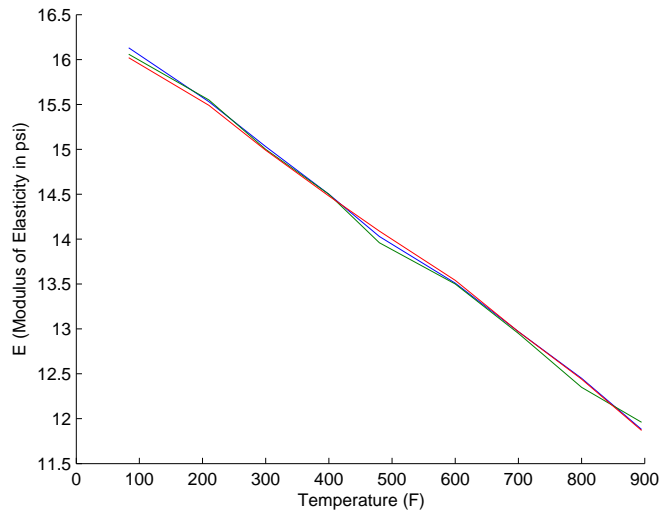
Figure 3-1: Modulus of elasticity for the first three dynamic modes of vibration for a free-free beam of titanium.

In Figure 3-1, the moduli for the three modes are nearly identical. The temperature range shown corresponds to the temperature range that will be used in the simulation section. Frequencies in Figure 3-2 correspond to a solid titanium beam, which will not correspond to the actual natural frequencies of the aircraft. The data shown in Figure 3-1 and Figure 3-2 are both from previous experimental work [47]. Using this data, different temperature gradients along the fuselage are introduced into the model and affect the structural properties of the HSV. The simulations in Chapter 4 and Chapter 5 use linearly decreasing gradients from the nose to the tail section. It's expected that the nose will be the hottest part of the structure due to aerodynamic heating behind the bow shock wave. Thermostructural dynamics are calculated under the assumption that there are nine constant-temperature sections in the aircraft [6] as shown in Figure 3-3. Since the aircraft is 100 feet long, the length of each of the nine sections is approximately 11.1 feet.
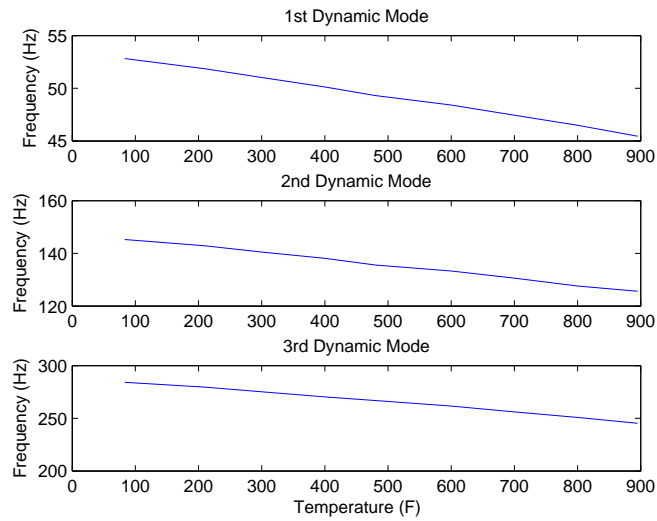
Figure 3-2: Frequencies of vibration for the first three dynamic modes of a free-free titanium beam.
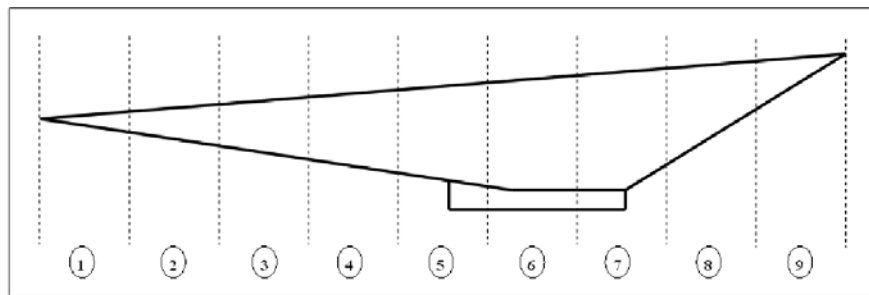
Figure 3-3: Nine constant temperature sections of the HSV used for temperature profile modeling.

Table 3-1: Natural frequencies for 5 linear temperature profiles (Nose/Tail) in degrees F. Percent difference is the difference between the maximum and minimum frequencies divided by the minimum frequency.

Mode	900/500	800/400	700/300	600/200	500/100	% Difference
1 (Hz)	23.0	23.5	23.9	24.3	24.7	7.39 %
2 (Hz)	49.9	50.9	51.8	52.6	53.5	7.21 %
3 (Hz)	98.9	101.0	102.7	104.4	106.2	7.38 %

The structural modes and frequencies are calculated using an assumed modes method with finite element discretization, including vehicle mass distribution and inertia effects. The result of this method is the generalized mode shapes and mode frequencies for the HSV. Because the beam is non-uniform in temperature, the modulus of elasticity is also non-uniform, which produces asymmetric mode shapes. An example of the asymmetric mode shapes is shown in Figure 3-5 and the asymmetry is due to variations in E resulting from the fact that each of the nine fuselage sections (see Figure 3-3) has a different temperature and hence different flexible dynamic properties. An example of some of the mode frequencies are provided in Table 1, which shows the variation in the natural frequencies for five decreasing linear temperature profiles shown in Figure 3-4. For all three natural modes, Table 3-1 shows that the natural frequency for the first temperature profile is almost 7% lower than that of the fifth temperature profile.

The temperature profile in a HSV is a complex function of the state history, structural properties, thermal protection system, etc. For the simulations in Chapter 4 and Chapter 5, the temperature profile is assumed to be a linear function that decreases from the nose to the tail of the aircraft. The linear profiles are then varied to span a preselected design space. Rather than attempting to model a physical temperature gradient for some vehicle design, the temperature profile in the simulations in Chapter 4 and Chapter 5 is intended to provide an aggressive temperature dependent profile to examine the robustness of the controller to such fluctuations.
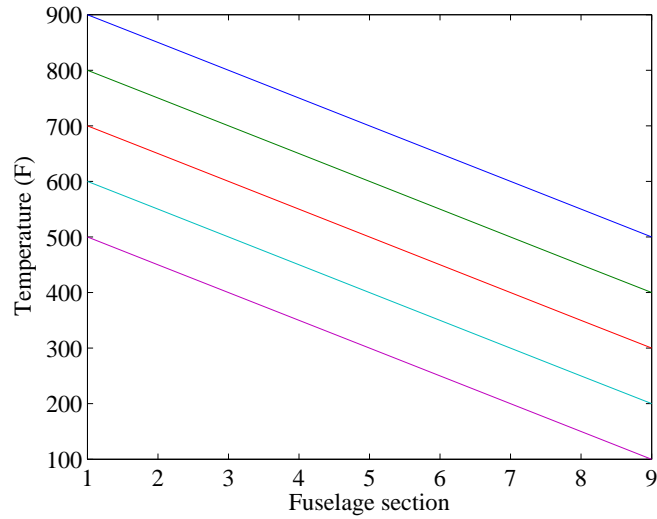
Figure 3-4: Linear temperature profiles used to calculate values shown in Table 3-1.
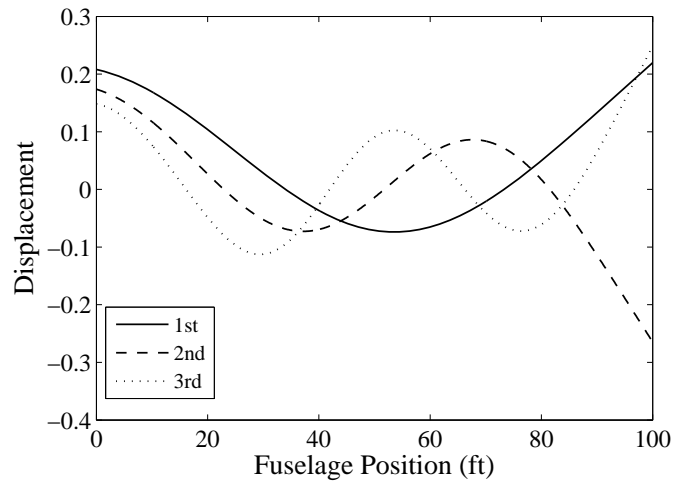
Figure 3-5: Asymetric mode shapes for the hypersonic vehicle. The percent difference was calculated based on the maximum minus the minimum structural frequencies divided by the minimum.

3.4   Conclusion

This chapter explains the overall flight and structural dynamics for a HSV, in the presence of different temperature profiles. These dynamics are important to understand because changes in the temperature profile modify the dynamics, hence can be modeled as additive parameter disturbances. In the following chapters, the HSV dynamics will be reduced to a LPV system with an additive disturbance, and the controller from Chapter 2 will be applied. The temperature profiles will act as the parameter variations. This chapter was meant to briefly introduce the overall system and explain the structural modes, shapes, and frequencies. Data was shown to motivate the fact that changes in temperature substantially affect the overall dynamics.

CHAPTER 4
LYAPUNOV-BASED EXPONENTIAL TRACKING CONTROL OF A HYPERSONIC AIRCRAFT WITH AEROTHERMOELASTIC EFFECTS

4.1 Introduction

The design of guidance and control systems for airbreathing hypersonic vehicles (HSV) is challenging because the dynamics of the HSV are complex and highly coupled [10], and temperature-induced stiffness variations impact the structural dynamics [21]. The structural dynamics, in turn, affect the aerodynamic properties. Vibration in the forward fuselage changes the apparent turn angle of the flow, which results in changes in the pressure distribution over the forebody of the aircraft. The resulting changes in the pressure distribution over the aircraft manifest themselves as thrust, lift, drag, and pitching moment perturbations [10]. To develop control laws for the longitudinal dynamics of a HSV capable of compensating for these structural and aerothermoelastic effects, structural temperature variations and structural dynamics must be considered.

Aerothermoelasticity is the response of elastic structures to aerodynamic heating and loading. Aerothermoelastic effects cannot be ignored in hypersonic flight, because such effects can destabilize the HSV system [21]. A loss of stiffness induced by aerodynamic heating has been shown to potentially induce dynamic instability in supersonic/hypersonic flight speed regimes [1]. Yet active control can be used to expand the flutter boundary and convert unstable limit cycle oscillations (LCO) to stable LCO [1]. An active structural controller was developed [26], which accounts for variations in the HSV structural properties resulting from aerothermoelastic effects. The control design [26] models the structural dynamics using a LPV framework, and states the benefits to using the LPV framework are two-fold: the dynamics can be represented as a single model, and controllers can be designed that have affine dependency on the operating parameters.

Previous publications have examined the challenges associated with the control of HSVs. For example, HSV flight controllers are designed using genetic algorithms to search a design parameter space where the nonlinear longitudinal equations of motion contain

uncertain parameters [4, 30, 49]. Some of these designs utilize Monte Carlo simulations to estimate system robustness at each search iteration. Another approach [4] is to use fuzzy logic to control the attitude of the HSV about a single low end flight condition. While such approaches [4, 30, 49] generate stabilizing controllers, the procedures are computationally demanding and require multiple evaluation simulations of the objective function and have large convergent times. An adaptive gain-scheduled controller [55] was designed using estimates of the scheduled parameters, and a semi-optimal controller is developed to adaptively attain H_∞ control performance. This controller yields uniformly bounded stability due to the effects of approximation errors and algorithmic errors in the neural networks. Feedback linearization techniques have been applied to a control-oriented HSV model to design a nonlinear controller [32]. The model [32] is based on a previously developed [8] HSV longitudinal dynamic model. The control design [32] neglects variations in thrust lift parameters, altitude, and dynamic pressure. Linear output feedback tracking control methods have been developed [44], where sensor placement strategies can be used to increase observability, or reconstruct full state information for a state-feedback controller. A robust output feedback technique is also developed for the linear parameterizable HSV model, which does not rely on state observation. A robust setpoint regulation controller [17] is designed to yield asymptotic regulation in the presence of parametric and structural uncertainty in a linear parameterizable HSV system.

An adaptive controller [19] was designed to handle (linear in the parameters) modeling uncertainties, actuator failures, and non-minimum phase dynamics [17] for a HSV with elevator and fuel ratio inputs. Another adaptive approach [41] was recently developed with the addition of a guidance law that maintains the fuel ratio within its choking limits. While adaptive control and guidance control strategies for a HSV are investigated [17, 19, 41], neither addresses the case where dynamics include unknown and unmodeled disturbances. There remains a need for a continuous controller, which is capable of achieving exponential tracking for a HSV dynamic model containing aerothermoelastic effects

and unmodeled disturbances (i.e., nonvanishing disturbances that do not satisfy the linear in the parameters assumption).

In the context of the aforementioned literature, the contribution of the current effort (and the preliminary effort by the authors [52]) is the development of a controller that achieves exponential model reference output tracking despite an uncertain model of the HSV that includes nonvanishing exogenous disturbances. A nonlinear temperature-dependent parameter-varying state-space representation is used to capture the aerothermoelastic effects and unmodeled uncertainties in a HSV. This model includes an unknown parameter-varying state matrix, an uncertain parameter-varying non-square (column deficient) input matrix, and a nonlinear additive bounded disturbance. To achieve an exponential tracking result in light of these disturbances, a robust, continuous Lyapunov-based controller is developed that includes a novel implicit learning characteristic that compensates for the nonvanishing exogenous disturbance. That is, the use of the implicit learning method enables the first exponential tracking result by a continuous controller in the presence of the bounded nonvanishing exogenous disturbance. To illustrate the performance of the developed controller during velocity, angle of attack, and pitch rate tracking, simulations for the full nonlinear model [10] are provided that include aerothermoelastic model uncertainties and nonlinear exogenous disturbances whose magnitude is based on airspeed fluctuations.

4.2 HSV Model

The dynamic model used for the subsequent control design is based on a reduction of the dynamics in (3–1)-(3–6) to the following combination of linear-parameter-varying (LPV) state matrices and additive disturbances arising from unmodeled effects as

$$\dot{x} = A\left(\rho\left(t\right)\right)x + B\left(\rho\left(t\right)\right)u + f\left(t\right) \tag{4–1}$$

$$y = Cx. \tag{4–2}$$

In (4–1) and (4–2), $x(t) \in \mathbb{R}^{11}$ is the state vector, $A(\rho(t)) \in \mathbb{R}^{11 \times 11}$ denotes a linear parameter varying state matrix, $B(\rho(t)) \in R^{11 \times 3}$ denotes a linear parameter varying input matrix, $C \in \mathbb{R}^{3 \times 11}$ denotes a known output matrix, $u(t) \in \mathbb{R}^3$ denotes a vector of 3 control inputs, $\rho(t)$ represents the unknown time-dependent parameters, $f(t) \in \mathbb{R}^{11}$ represents a time-dependent unknown, nonlinear disturbance, and $y(t) \in \mathbb{R}^3$ represents the measured output vector of size 3.

4.3   Control Objective

The control objective is to ensure that the output $y(t)$ tracks the time-varying output generated from the reference model like stated in Chapter 2. To quantify the control objective, an output tracking error, denoted by $e(t) \in \mathbb{R}^3$, is defined as

$$e \triangleq y - y_m = C(x - x_m). \tag{4–3}$$

To facilitate the subsequent analysis, a filtered tracking error denoted by $r(t) \in \mathbb{R}^3$, is defined as

$$r \triangleq \dot{e} + \gamma e \tag{4–4}$$

where $\gamma \in \mathbb{R}^3$ is a positive definite diagonal, constant control gain matrix, and is selected to place a relative weight on the error state verses its derivative. Based on the control design presented in Chapter 2 the control input is designed as

$$u = -k_\Gamma (CB_0)^{-1} [(k_s + I_{3 \times 3}) e(t) - (k_s + I_{3 \times 3}) e(0) + \upsilon(t)] \tag{4–5}$$

where $\upsilon(t) \in \mathbb{R}^3$ is an implicit learning law with an update rule given by

$$\dot{\upsilon}(t) = k_u \|u(t)\| sgn(r(t)) + (k_s + I_{3 \times 3}) \gamma e(t) + k_\gamma sgn(r(t)) \tag{4–6}$$

and $k_\Gamma, k_u, k_s, k_\gamma \in \mathbb{R}^{3 \times 3}$ denote positive definite, diagonal constant control gain matrices, $B_0 \in \mathbb{R}^{11 \times 3}$ represents a known nominal input matrix, $sgn(\cdot)$ denotes the standard signum function where the function is applied to each element of the vector argument, and $I_{3 \times 3}$ denotes a 3×3 identity matrix. To illustrate the performance of the controller

and practicality of the assumptions, a numerical simulation was performed on the full nonlinear longitudinal equations of motion [10] given in (3–1)-(3–6). The control inputs were selected as $u = \begin{bmatrix} \delta_e(t) & \delta_c(t) & \phi_f(t) \end{bmatrix}^T$, as in previous research [41], where $\delta_e(t)$ and $\delta_c(t)$ denote the elevator and canard deflection angles, respectively, $\phi_f(t)$ is the fuel equivalence ratio. The diffuser area ratio is left at its operational trim condition without loss of generality ($A_d(t) = 1$). The reference outputs were selected as maneuver oriented outputs of velocity, angle of attack, and pitch rate as $y = \begin{bmatrix} V(t) & \alpha(t) & Q(t) \end{bmatrix}^T$ where the output and state variables are introduced in (3–1)-(3–5). In addition, the proposed controller could be used to control other output states such as altitude provided the following condition is valid. The auxiliary matrix $\tilde{\Omega}(\rho(t)) \in \mathbb{R}^{q \times q}$ is defined as

$$\tilde{\Omega} \triangleq CBk_\Gamma (CB_0)^{-1} \tag{4–7}$$

where $\tilde{\Omega}(\rho(t))$ can be separated into diagonal (i.e., $\Lambda(\rho(t)) \in \mathbb{R}^{q \times q}$) and off-diagonal (i.e., $\Delta(\rho(t)) \in \mathbb{R}^{q \times q}$) components as

$$\tilde{\Omega} = \Lambda + \Delta. \tag{4–8}$$

The uncertain matrix $\tilde{\Omega}(\rho(t))$ is diagonally dominant in the sense that

$$\lambda_{\min}(\Lambda) - \|\Delta\|_{i\infty} > \varepsilon \tag{4–9}$$

where $\varepsilon \in \mathbb{R}^+$ is a known constant. While this assumption cannot be validated for a generic HSV, the condition can be checked (within some certainty tolerances) for a given aircraft. Essentially, this condition indicates that the nominal value B_0 must remain within some bounded region of B. In practice, bands on the variation of B should be known, for a particular aircraft under a set of operating conditions, and this band could be used to check the sufficient conditions. For the specific HSV example this Chapter simulates, the assumtion in 4–9 is valid.

4.4 Simulation Results

The HSV parameters used in the simulation are $m = 75,000 \ lbs$, $I_{yy} = 86723$ $lbs \cdot ft^2$, and $g = 32.174 \ ft/s^2$.as defined in (3–1)-(3–6). The simulation was executed for 35 seconds to sufficiently cycle through the different temperature profiles. Other vehicle parameters in the simulation are functions of the temperature profile. Linear temperature profiles between the forebody (i.e., $T_{fb} \in [450, 900]$) and aftbody (i.e., $T_{ab} \in [100, 800]$) were used to generate elastic mode shapes and frequencies by varying the linear gradients as

$$T_{fb}(t) = 675 + 225 \cos\left(\frac{\pi}{10}t\right) \qquad T_{ab}(t) = \begin{cases} 450 + 350 \cos\left(\frac{\pi}{3}t\right) & \text{if } T_{fb}(t) > T_{ab}(t) \\ T_{fb}(t) & \text{otherwise.} \end{cases}$$

$$(4\text{–}10)$$

Figure 4-1 shows the temperature variation as a function of time. The irregularities seen in the aftbody temperatures occur because the temperature profiles were adjusted to ensure the tail of the aircraft was equal or cooler than the nose of the aircraft according to bow shockwave thermodynamics. While the shockwave thermodynamics motivated the need to only consider the case when the tail of the aircraft was equal or cooler than the nose of the aircraft, the shape of the temperature profile is not physically motivated. Specifically, the frequencies of oscillation in (4–10) were selected to aggressively span the available temperature ranges. These temperature profiles are not motivated by physical temperature gradients, but motivated by the desire to generate a temperature disturbance to illustrate the controller robustness to the temperature gradients. The simulation assumes the damping coefficient remains constant for the structural modes $(\zeta_i = 0.02)$.

In addition to thermoelasticity, a bounded nonlinear disturbance was added to the dynamics as

$$f = \begin{bmatrix} f_{\dot{V}} & f_{\dot{\alpha}} & f_{\dot{Q}} & 0 & 0 & 0 & f_{\ddot{\eta}1} & 0 & f_{\ddot{\eta}2} & 0 & f_{\ddot{\eta}3} \end{bmatrix}^T, \qquad (4\text{–}11)$$
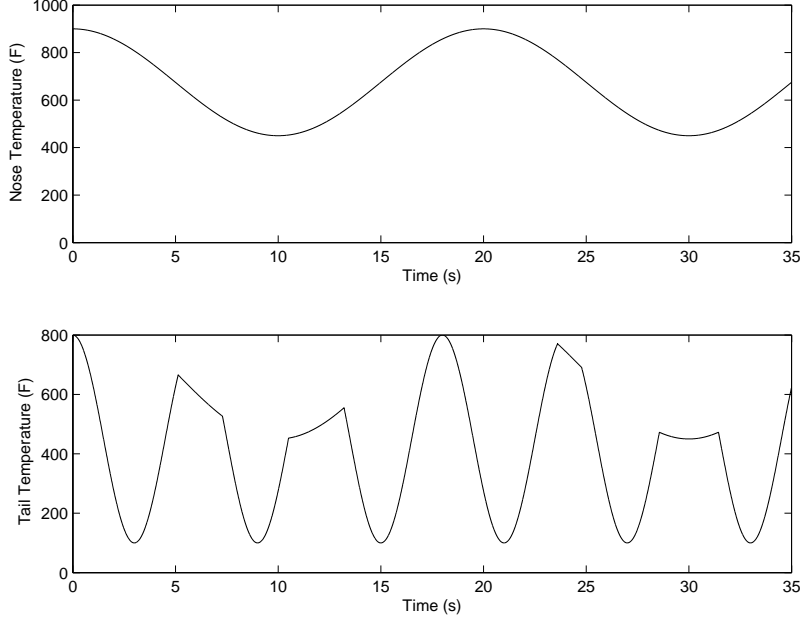
Figure 4-1: Temperature variation for the forebody and aftbody of the hypersonic vehicle as a function of time.

where $f_{\dot{V}}(t) \in \mathbb{R}$ denotes a longitudinal acceleration disturbance, $f_{\dot{\alpha}}(t) \in \mathbb{R}$ denotes a angle of attack rate of change disturbance, $f_{\dot{Q}}(t) \in \mathbb{R}$ denotes an angular acceleration disturbance, and $f_{\ddot{\eta}1}(t), f_{\ddot{\eta}2}(t), f_{\ddot{\eta}3}(t), \in \mathbb{R}$ denote structural mode acceleration disturbances. The disturbances in (4–11) were generated as an arbitrary exogenous input (i.e., unmodeled nonvanishing disturbance that does not satisfy the linear in the parameters assumption) as depicted in Figure 4-2. However, the magnitudes of the disturbances were motivated by the scenario of a 300 ft/s change in airspeed. The disturbances are not designed to mimic the exact effects of a wind gust, but to demonstrate the proposed controller's robustness with respect to realistically scaled disturbances. Specifically, a relative force disturbance is determined by comparing the drag force D at Mach 8 at $85,000$ ft (i.e., 7355 ft/s) with the drag force after adding a 300 ft/s (e.g., a wind gust) disturbance. Using Newton's second law and dividing the drag force differential ΔD by the mass of the HSV m, a realistic upper bound for an acceleration disturbance $f_{\dot{V}}(t)$ was determined. Similarly, the same procedure can be performed, to compare the change in pitching moment ΔM caused by a 300 ft/s head wind gust. By dividing the moment differential by the moment of
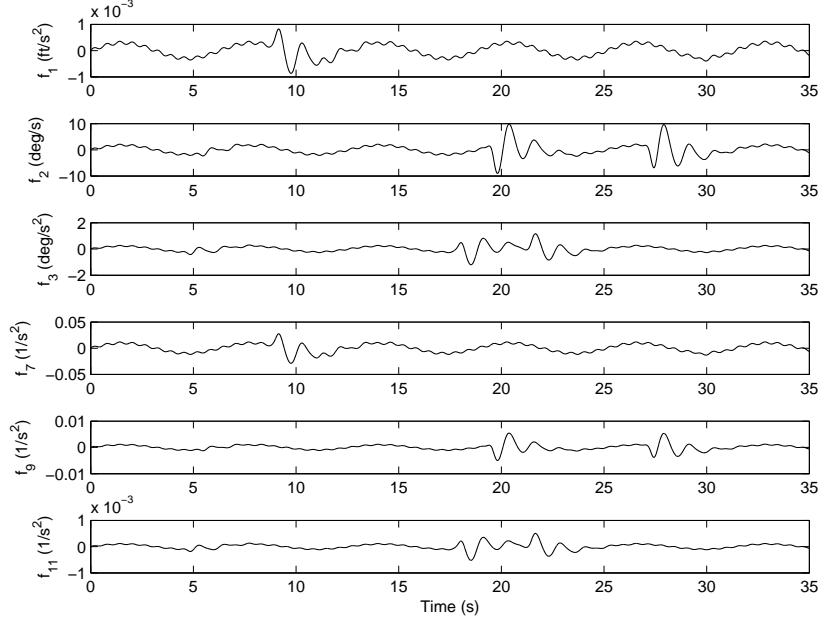
Figure 4-2: In this figure, f_i denotes the ith element in the disturbance vecor f. Disturbances from top to bottom: velocity $f_{\dot{V}}$, angle of attack $f_{\dot{\alpha}}$, pitch rate $f_{\dot{Q}}$, the 1st elastic structural mode $\ddot{\eta}_1$, the 2nd elastic structural mode $\ddot{\eta}_2$, and the 3rd elastic structural mode $\ddot{\eta}_3$, as described in (4–11).

inertia of the HSV I_{yy}, a realistic upper bound for $f_{\dot{Q}}(t)$ can be determined. To calculate a reasonable angle of attack disturbance magnitude, a vertical wind gust of 300 ft/s is considered. By taking the inverse tangent of the vertical wind gust divided by the forward velocity at Mach 8 and 85,000 ft, an upper bound for the angle of attack disturbance $f_{\dot{\alpha}}(t)$ can be determined. Disturbances for the structural modes $f_{\ddot{\eta}i}(t)$ were placed on the acceleration terms with $\ddot{\eta}_i(t)$, where each subsequent mode is reduced by a factor of 10 relative to the first mode, see Figure 4-2.

The proposed controller is designed to follow the outputs of a well behaved reference model. To obtain these outputs, a reference model that exhibited favorable characteristics was designed from a static linearized dynamics model of the full nonlinear dynamics [10]. The reference model outputs are shown in Figure 4-3. The velocity reference output follows a 1000 ft/s smooth step input, while the pitch rate performs several ± 1 °/s maneuvers. The angle of attack stays within ± 2 degrees.

46
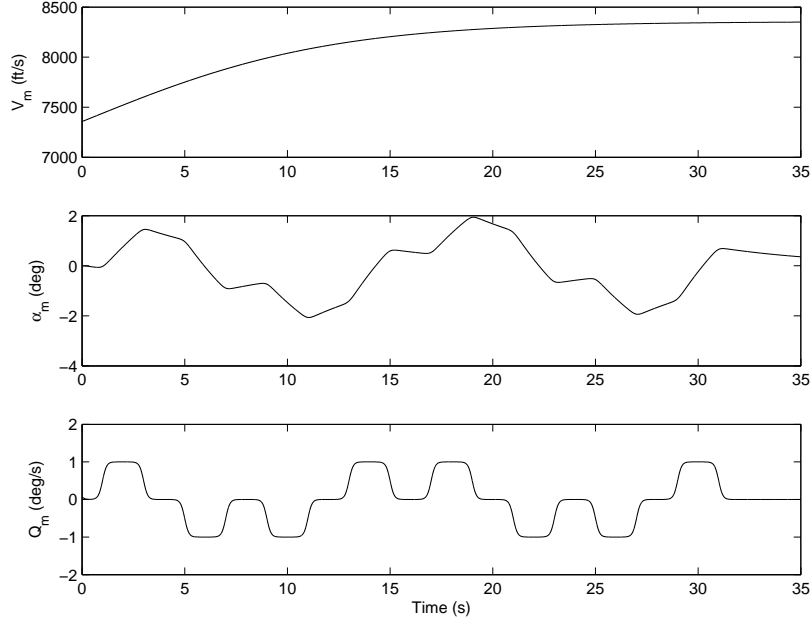
Figure 4-3: Reference model ouputs y_m, which are the desired trajectories for top: velocity $V_m(t)$, middle: angle of attack $\alpha_m(t)$, and bottom: pitch rate $Q_m(t)$.

The control gains for (4–3)-(4–4) and (4–5)-(4–6) are selected as

$$\gamma = diag\{10, 10\} \qquad k_s = diag\{5, 1, 300\} \qquad k_u = diag\{0.01, 0.001, 0.01\}$$

$$k_\gamma = diag\{0.1, 0.01, 0.1\} \qquad k_\Gamma = diag\{1, 0.5, 1\}. \tag{4–12}$$

The control gains in (4–12) were obtained using the same method as in Chapter 5. In contrast to this suboptimal approach used, the control gains could have been adjusted using more methodical approaches as described in various survey papers on the topic [24, 46].

The C matrix and knowledge of some nominal B_0 matrix must be known. The C matrix is given by:

$$C = \begin{bmatrix} 1 & 0 & 0 & 0 & 0 & 0 & 0 & 0 & 0 & 0 & 0 \\ 0 & 1 & 0 & 0 & 0 & 0 & 0 & 0 & 0 & 0 & 0 \\ 0 & 0 & 1 & 0 & 0 & 0 & 0 & 0 & 0 & 0 & 0 \end{bmatrix} \tag{4–13}$$
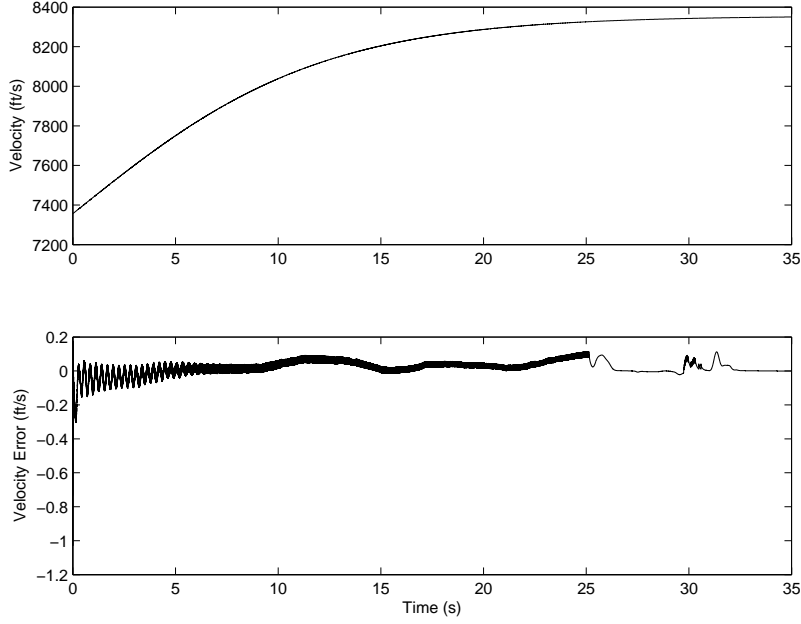
Figure 4-4: Top: velocity $V(t)$, bottom: velocity tracking error $e_V(t)$.

for the output vector of (4–2), and the B_0 matrix is selected as

$$
B_0 = \begin{bmatrix} -32.69 & -0.017 & -9.07 & 0 & 0 & 0 & 2367 & 0 & -1132 & 0 & -316 \\ 25.72 & -0.011\,1 & 9.39 & 0 & 0 & 0 & 3189 & 0 & 2519 & 0 & 2067 \\ 42.84 & -0.001\,6 & 0.052\,7 & 0 & 0 & 0 & 42.13 & 0 & 92.12 & 0 & -80.0 \end{bmatrix}^T \tag{4–14}
$$

based on a linearized plant model about some nominal conditions.

The HSV has an initial velocity of Mach 7.5 at an altitude of $85,000\ ft$. The velocity, and velocity tracking errors are shown in Figure 4-4. The angle of attack and angle of attack tracking error is shown in Figure 4-5. The pitch rate and pitch tracking error is shown in Figure 4-6. The control effort required to achieve these results is shown in Figure 4-7. In addition to the output states, other states such as altitude and pitch angle are shown in Figure 4-8. The structural modes are shown in Figure 4-9.

4.5   Conclusion

This result represents the first ever application of a continuous, robust model reference control strategy for a hypersonic vehicle system with additive bounded disturbances
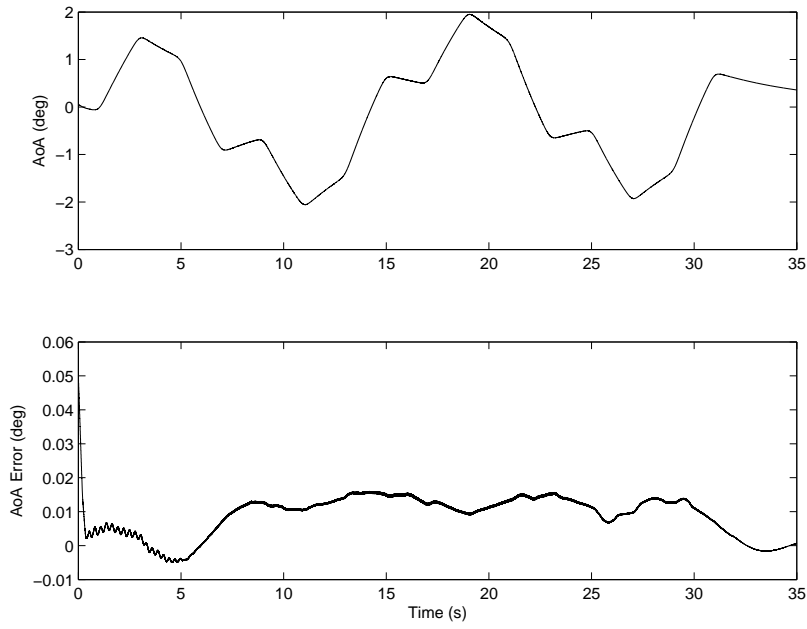
Figure 4-5: Top: angle of attack $\alpha(t)$, bottom: angle of attack tracking error $e_\alpha(t)$.
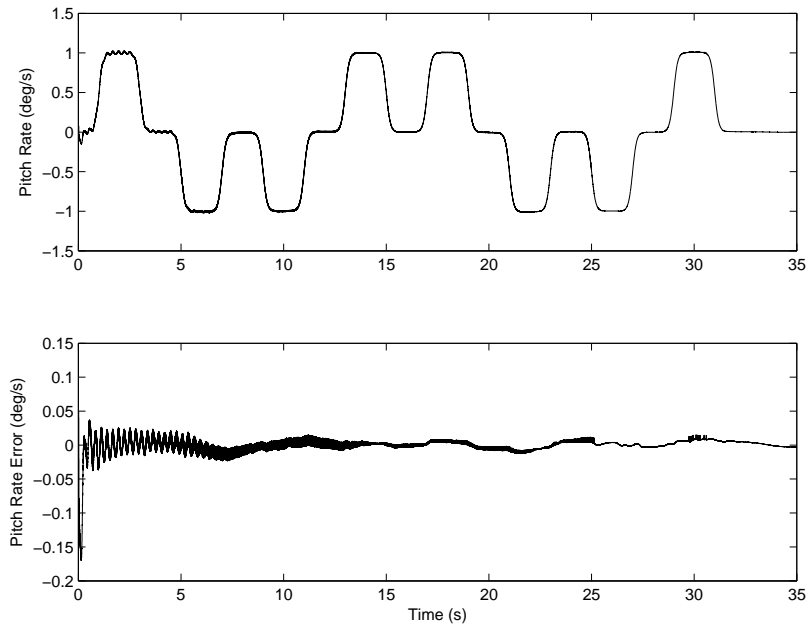
Figure 4-6: Top: pitch rate $Q(t)$, bottom: pitch rate tracking error $e_Q(t)$.
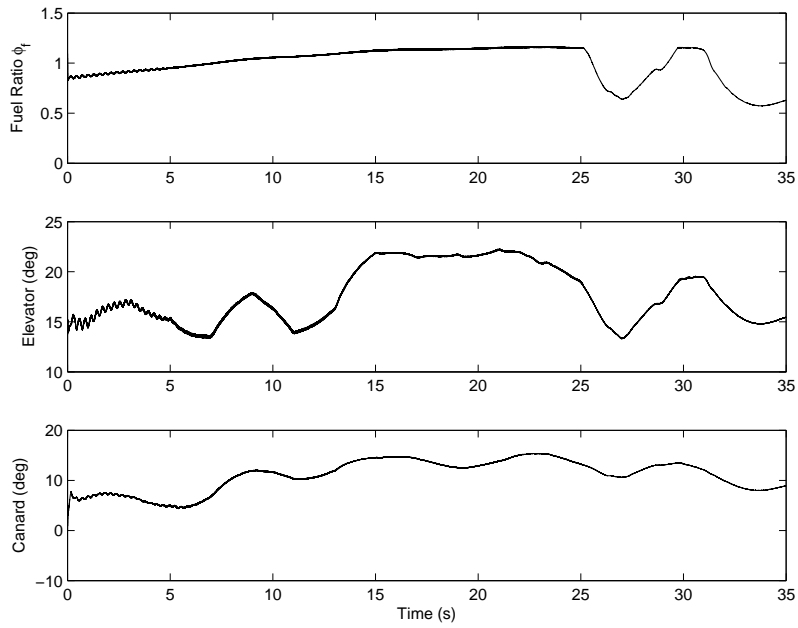
Figure 4-7: Top: fuel equivalence ratio ϕ_f. Middle: elevator deflection δ_e. Bottom: Canard deflection δ_c.
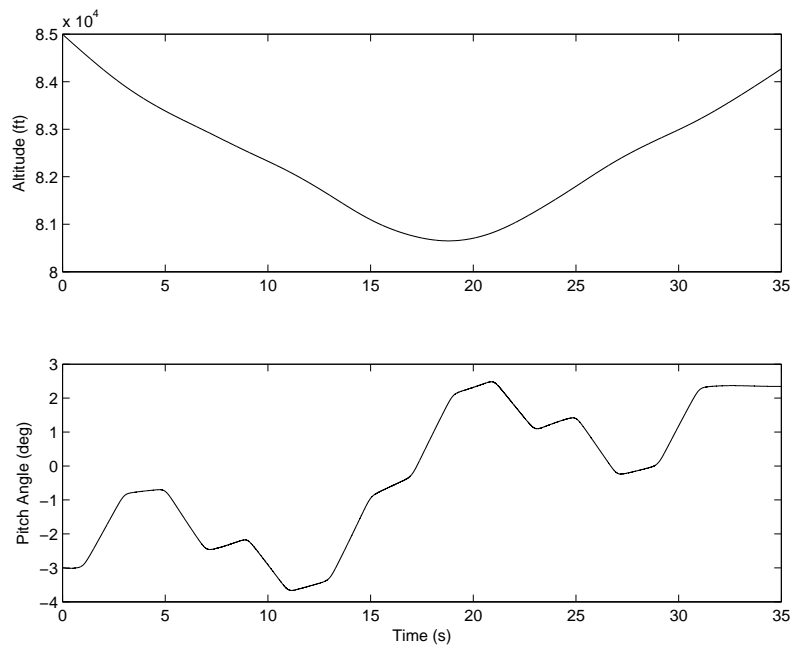
Figure 4-8: Top: altitude $h(t)$, bottom: pitch angle $\theta(t)$.
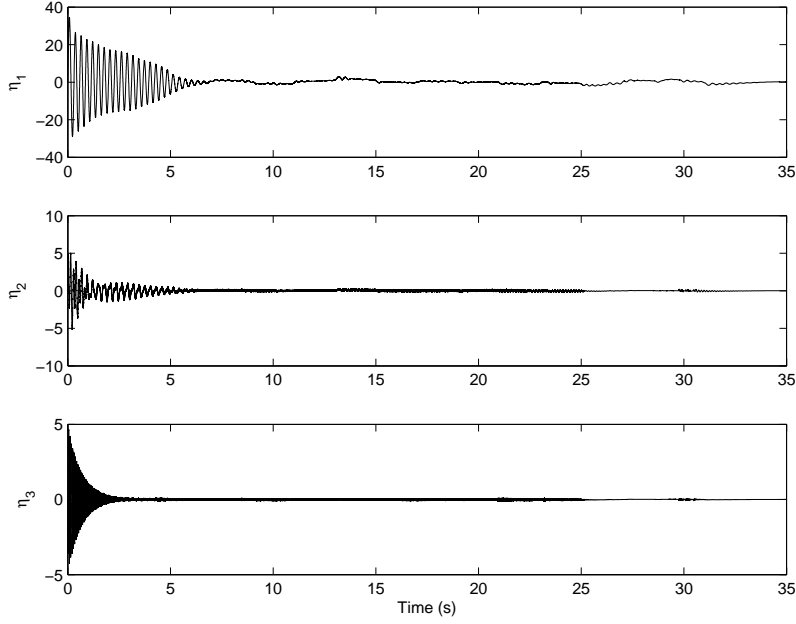
Figure 4-9: Top: 1st structural elastic mode η_1. Middle: 2nd structural elastic mode η_2. Bottom: 3rd structural elastic mode η_3.

and aerothermoelastic effects, where the control input is multiplied by an uncertain, column deficient, parameter-varying matrix. A potential drawback of the result is that the control structure requires that the product of the output matrix with the nominal control matrix be invertible. For the output matrix and nominal matrix, the elevator and canard deflection angles and the fuel equivalence ratio can be used for tracking outputs such as the velocity, angle of attack, and pitch rate or velocity and the flight path angle, or velocity, flight path angle and pitch rate. Yet, these controls can not be applied to solve the altitude tracking problem because the altitude is not directly controllable and the product of the output matrix with the nominal control matrix is singular. However, the integrator backstepping approach that has been examined in other recent results for the hypersonic vehicle could potentially be incorporated in the control approach to address such objectives. A Lyapunov-based stability analysis is provided to verify the exponential tracking result. Although the controller was developed using a linear parameter varying model of the hypersonic vehicle, simulation results for the full nonlinear model with temperature variations and exogenous disturbances illustrate the boundedness of the controller with

favorable transient and steady state tracking errors. These results indicate that the LPV model with exogenous disturbances is a reasonable approximation of the dynamics for the control development.

CHAPTER 5
CONTROL PERFORMANCE VARIATION DUE TO NONLINEAR AEROTHERMOELASTICITY IN A HYPERSONIC VEHICLE: INSIGHTS FOR STRUCTURAL DESIGN

5.1   Introduction

Typically, controllers are developed to achieve some performance metrics for a given HSV model. However, improved performance and robustness to thermal gradients could result if the structural design and control design were optimized in unison. Along this line of reasoning in [16, 23], the advantage of correctly placing the sensors is discussed, representing a move towards implementing a control friendly design. A previous control oriented design analysis in [6] states that simultaneously optimizing both the structural dynamics and control is an intractable problem, but that control-oriented design may be performed by considering the closed-loop performance of an optimal controller on a series of different open-loop design models. The best performing design model is then said to have the optimal dynamics in the sense of controllability.

Knowledge of the better performing thermal gradients can provide design engineers insight to properly weight the HSV's thermal protection system for both steady-state and transient flight. The preliminary work in [6] provides a control-oriented design architecture by investigating control performance variations due to thermal gradients using an $\mathcal{H}_\infty$ controller. Chapter 5 seeks to extend the control oriented design concept to examine control performance variations for HSV models that include nonlinear aerothermoelastic disturbances. Given these disturbances, Chapter 5 focuses on examining control performance variations for our previous model reference robust controller in [52] and previous chapters to achieve a nonlinear control-oriented analysis with respect to thermal gradients. By analyzing the control error and input norms over a wide range of temperature profiles an optimal temperature profile range is suggested. Based on preliminary work done in [50], a number of linear temperature profile models are examined for insight into the structural design. Specifically, the full set of nonlinear flight dynamics will be used and control effort,

53

errors, and transients such as steady-state time and peak to peak error will be examined across the design space.

5.2   Dynamics and Controller

The HSV dynamics used in this chapter are the same is in Chapter 3 and equations (3–1)-(3–6). Similarly as in the results in Chapter 4, the dynamics in (3–1)-(3–6) are reduced to the linear parameter model used in (2–1) and (2–2) with $p = q = 2$. For the control-oriented design analysis, a number of different linear profiles are chosen [6, 50] with varying nose and tail temperatures as illustrated in Figure 5-1. This set of profiles define the space from which the control-oriented analysis will be performed. As seen in Figure 5-1, the temperature profiles are linear and decreasing towards the tail. These profiles are realistic based on shock formation at the front of the vehicle and that the temperatures are within the expected range for hypersonic flight. Based on previous
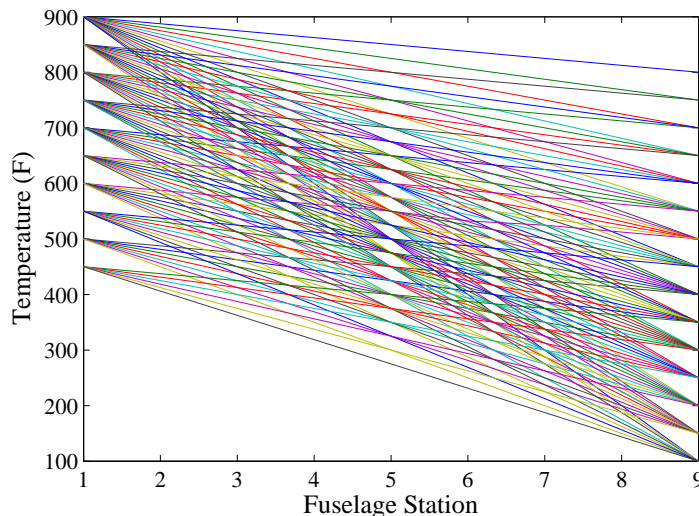
Figure 5-1: HSV surface temperature profiles. $T_{nose} \in [450°F, 900°F]$, and $T_{tail} \in [100°F, 800°F]$.

control development in [52] and in the previous Chapters, the control input is designed as

$$u = -k_\Gamma \left(CB_0\right)^{-1} \left[\left(k_s + I_{3\times3}\right) e\left(t\right) - \left(k_s + I_{3\times3}\right) e\left(0\right) + \upsilon\left(t\right)\right] \qquad (5\text{–}1)$$

where $\upsilon(t) \in \mathbb{R}^2$ is an implicit learning law with an update rule given by

$$\dot{\upsilon}(t) = k_u \|u(\sigma)\| sgn(r(\sigma)) + (k_s + I_{3\times3})\gamma e(\sigma) + k_\gamma sgn(r(\sigma)) \qquad (5\text{--}2)$$

where $k_\Gamma, k_u, k_s, k_\gamma \in \mathbb{R}^{2\times2}$ denote positive definite, diagonal constant control gain matrices, $B_0 \in \mathbb{R}^{11\times2}$ represents a known nominal input matrix, $sgn(\cdot)$ denotes the standard signum function where the function is applied to each element of the vector argument, and $I_{2\times2}$ denotes a 2×2 identity matrix.

5.3   Optimization via Random Search and Evolving Algorithms

For each of the individual temperature profiles examined, the control gains k_Γ, k_u, k_s, k_γ, and γ in (5–1)-(5–2) were optimized for the specific plant model using a combination of random search and evolving algorithms. Since both the plant model simulation dynamics and the control scheme itself are nonlinear, traditional methods for linear gain tuning optimization could not be used. The selected method is a combination of a control gain random search space, combined with an evolving algorithm scheme which allows the search to find a nearest set of optimal control gains for each individual plant. This method allows one near-optimal controller/plant to be compared to the other near-optimal controller/plants and provides a more accurate way of comparing cases.

The first step in the control gain optimization search is a random initialization. For this numerical study, 1000 randomly selected sets of control gains are used for a given plant model. A 1000 initial random set was chosen to provide sufficient sampling to insure global convergence. The following section has a specific example case for one of the temperature profiles. After the 1000 control gain sets are selected, all the sets are simulated on the given plant model and the controller in (5–1) and (5–2) is applied to track a certain trajectory as well as reject disturbances. The trajectory and disturbances were chosen the same throughout the entire study so that the only variations will be due to the plant model and control gains. The example case section explicitly shows both the desired trajectory and the disturbances injected.

After the 1000 initial random control gain search is performed, the top five performing sets of control gains are chosen as the seeds for the evolving algorithm process. This process is repeated for four generations, each with the best five performing sets of control gains at each step. All evolving algorithms have some or all of the following characteristics: elitism, crossover, and random mutation. This particular numerical study uses all three as follows. The best five performing sets in each subsequent generation, are chosen as elite and move onto the next iteration step. From those five, each set of control gains is averaged with all other permutations of control gains in the elite set. For instance, if parent #1 is averaged with #2 to form an offspring set of control gains. Parent #1 is also averaged with parent #3 for a separate set of offspring control gains. In this way, all combinations of crossover are performed. The permutations of the five elite parents yield a total of 10 offspring.

The next generation contains the five elite parents from the generation before, as well as the 10 crossover offspring, for a total of 15. Each of these 15 sets of control gains is then mutated by a certain percentage. Based on preliminary numerical studies performed on this specific example, the random mutations were chosen to be 20% for the first two generations and 5% for the final two generations. This produced both global search in the beginning, and refinement at the end of the optimization procedure. The set of 15 remains, with the addition of 20 mutated sets for each of the 15. This gives a total control gain set for the next generation of search of 315. As stated, there are four evolving generations after the first 1000 random control sets. The combined number of simulations with different control gains performed for a single temperature profile case is 2260. These particular numbers were chosen based on preliminary trial optimization cases, with the goal to provide sufficient search to achieve convergence of a minimum for the cost function. The following section illustrates the entire procedure for a single temperature profile case.

The cost function is designed such that the errors and control inputs are the same order of magnitudes, so that they can more easily be added and interpreted. This is important because for example, the desired velocity is high (in the thousands of ft/s) and the desired pitch rate is small (fraction of radians). Explicitly, the cost function is taken as the sum of the control and error norms and is scaled as

$$\Omega_{err} = \left\| 100e_V \quad 1000\frac{180}{\pi}e_Q \right\|_2 \tag{5–3}$$

and

$$\Omega_{con} = \left\| \frac{180}{\pi}\delta_e \quad 10\phi_f \right\|_2 \tag{5–4}$$

where $e_V(t), e_Q(t) \in \mathbb{R}$ are the velocity and pitch rate errors, respectively, and $\delta_e(t), \phi_f(t) \in \mathbb{R}$ are the elevator and fuel ratio control inputs, respectively, and $\|\cdot\|_2$ denotes the standard 2-norm. The combined cost function is the sum of the individual components and can be explicitly written as

$$\Omega_{tot} = \Omega_{err} + \Omega_{con} \tag{5–5}$$

where Ω_{tot} is the cost value associated with all subsequent optimal gain selection.

5.4   Example Case

The HSV parameters used in the simulation are $m = 75,000$ lbs , $I_{yy} = 86723$ $lbs \cdot ft^2$, and $g = 32.174$ ft/s^2.as defined in (3–1)-(3–6). To illustrate how the random search and evolving optimization algorithms work, this section is provided as a detailed example. First the output tracking signal and disturbances are provided, followed by the optimization and convergence procedure. The goal of this section is to demonstrate that the specific number of elites, offspring, mutations, and generations listed in the previous section are justified in that the cost function shows asymptotic convergence to a minimum. The desired trajectory is shown in Figure 5-2 and the disturbance is depicted in Figure 5-3, where the magnitudes are chosen based on previous analysis performed in [52]. The example case is based on a temperature profile with $T_{nose} = 350°F$ and $T_{tail} = 200°F$. For
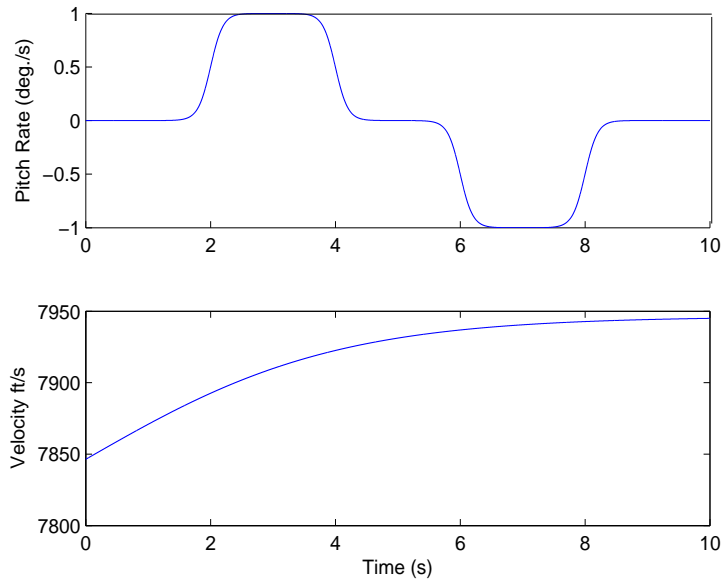
Figure 5-2: Desired trajectories: pitch rate Q (top) and velocity V (bottom).
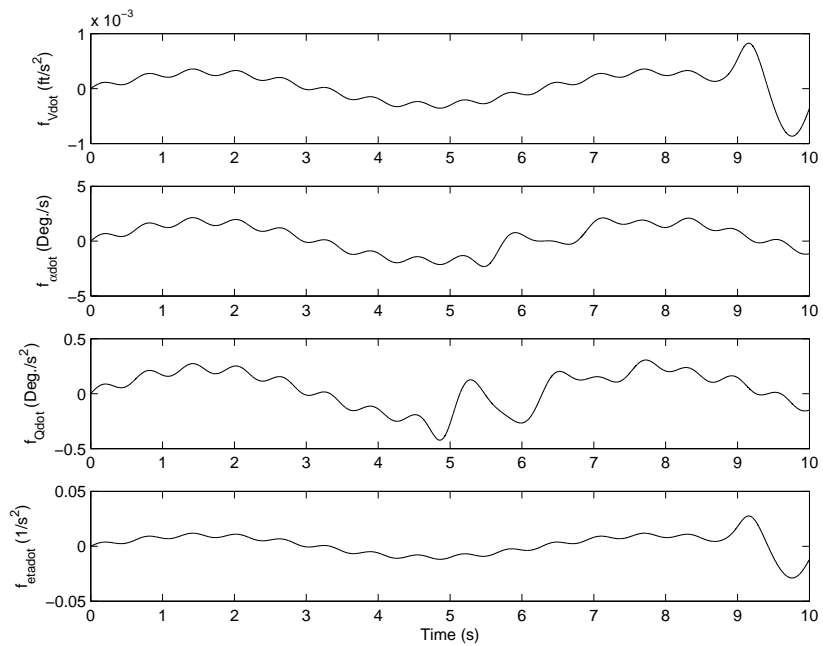
Figure 5-3: Disturbances for velocity V (top), angle of attack α (second from top), pitch rate Q (second from bottom) and the 1st structural mode (bottom).
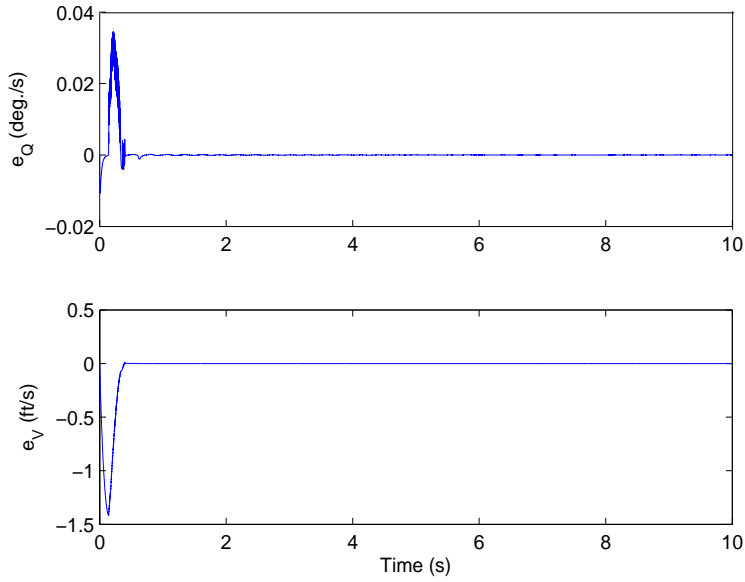
Figure 5-4: Tracking errors for the pitch rate Q in degrees/sec (top) and the velocity V in ft/sec (bottom).

this particular case, Figure 5-4 and Figure 5-5 show the tracking errors and control inputs, respectively, for the control gains

$$\gamma = \begin{bmatrix} 11.17 & 0 \\ 0 & 39.61 \end{bmatrix}, \quad k_s = \begin{bmatrix} 14.55 & 0 \\ 0 & 224.0 \end{bmatrix}, \quad k_u = \begin{bmatrix} 25.99 & 0 \\ 0 & 0.618 \end{bmatrix}$$

$$k_\gamma = \begin{bmatrix} 20.7 & 0 \\ 0 & 0.369 \end{bmatrix}, \quad k_\Gamma = \begin{bmatrix} 0.915 & 0 \\ 0 & 0.898 \end{bmatrix}. \tag{5-6}$$

The cost functions have values as seen in Figure 5-6. In Figure 5-6 the control input cost remains approximately the same, but as the control gains evolve, the error cost and hence total cost decrease asymptotically. The 1st five iterations correspond to the top five performers in the first 1000 random sample, and each subsequent five correspond to the top five for the subsequent evolution generations. To limit the optimization search design space, all simulations are performed with two inputs and two outputs. As indicated in the cost functions listed in (5-3)-(5-5), the inputs include the elevator deflection $\delta_e(t)$ and the fuel ratio $\phi_f(t)$, and the outputs are the velocity $V(t)$ and the pitch rate $Q(t)$.
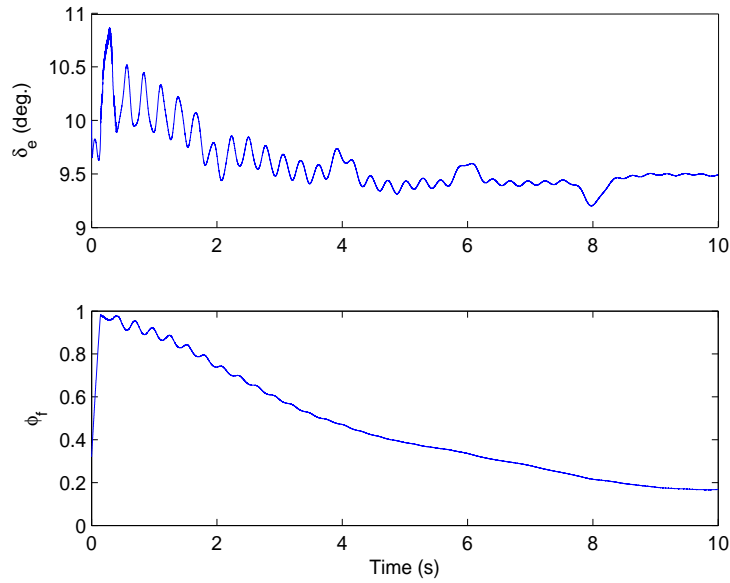
Figure 5-5: Control inputs for the elevator δ_e in degrees (top) and the fuel ratio ϕ_f (bottom).
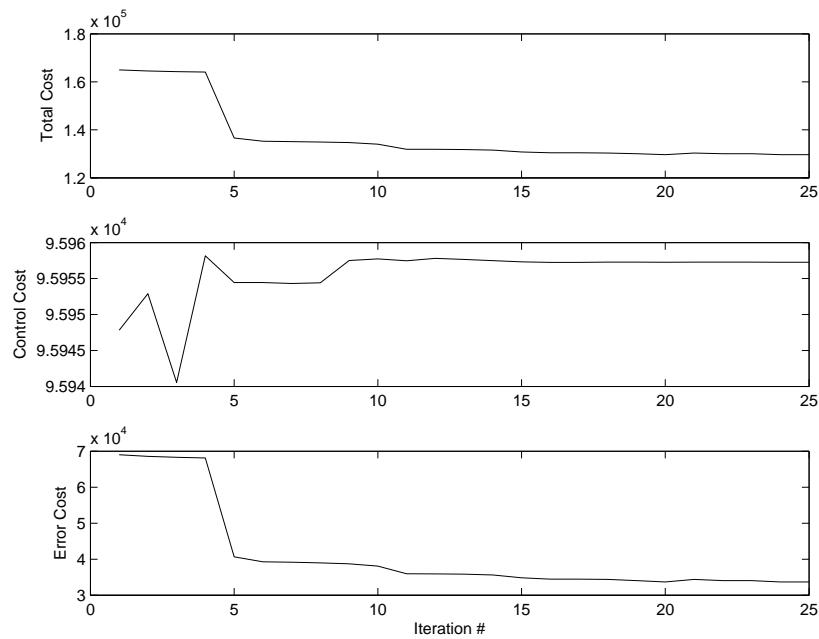
Figure 5-6: Cost function values for the total cost Ω_{tot} (top), the input cost Ω_{con} (middle) and the error cost Ω_{err} (bottom).

5.5 Results

The results of this section cover all the temperature profiles shown in Figure 5-1. The data presented includes the cost functions as well as other steady-state and transient data. Included in this analysis are the control cost function, the error cost function, the peak-to-peak transient response, the time to steady-state, and the steady-state peak-to-peak, for both control and error signals. Because the data contains noise, a smoothed version of each plot is also provided. The smoothed plots use a standard 2-dimensional filtering, where each point is averaged with its neighbors. For instance for some variable ω, the averaged data is generated as

$$\omega_{i,j} = \frac{(4\omega_{i,j} + \omega_{i+1,j} + \omega_{i-1,j} + \omega_{i,j+1} + \omega_{i,j-1})}{8}. \tag{5–7}$$

The averaging formula shown in (5–7) is used for filtering of all subsequent data. Also, note that the lower right triangle formation is due to the design space only containing temperature profiles where the nose is hotter than the tail. This is due to the assumption that because of aerodynamic heating from the extreme speeds of the HSV, that this will always be the case. These temperature profiles relate to the underlying structural temperature, not necessarily the skin surface temperature. Figure 5-7 and Figure 5-8 show the control cost function value Ω_{con}. Note that there is a global minimum, however also note for all of the control norms the total values are approximately the same. This data indicates that while other performance metrics varied widely as a function of temperature profile, the overall input cost remains approximately the same. In Figure 5-9 and Figure 5-10, the error cost is shown. Note that there is variability, but that there seems to be a region of smaller errors in the cooler section of the design space. Namely, where $T_{nose} \in [200, 600]^\circ F$ and $T_{tail} \in [100, 250]^\circ F$. Combining the control cost function with the error cost function yields the total cost function (and its filtered counterpart) depicted in Figure 5-11 (and Figure 5-12, respectively). The importance of this plot is that the total cost function was the criteria for which the control gains were optimized. In this
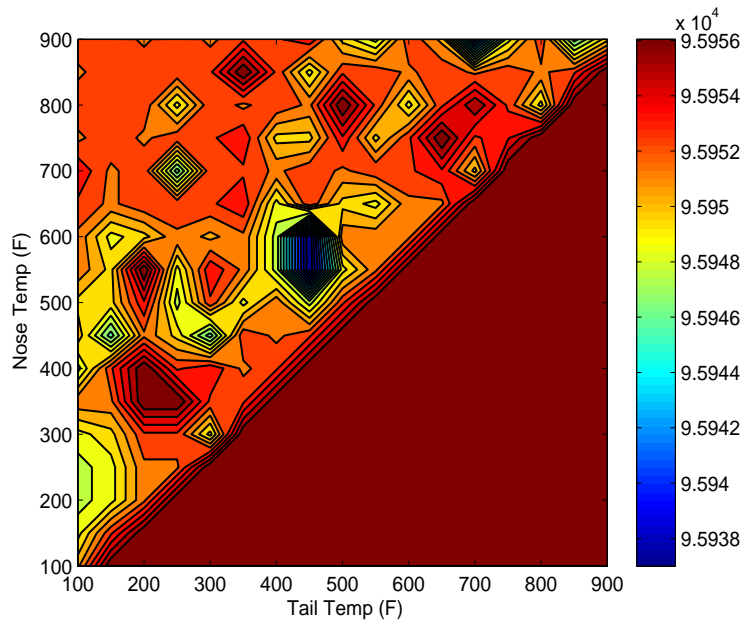
Figure 5-7: Control cost function Ω_{con} data as a function of tail and nose temperature profiles.
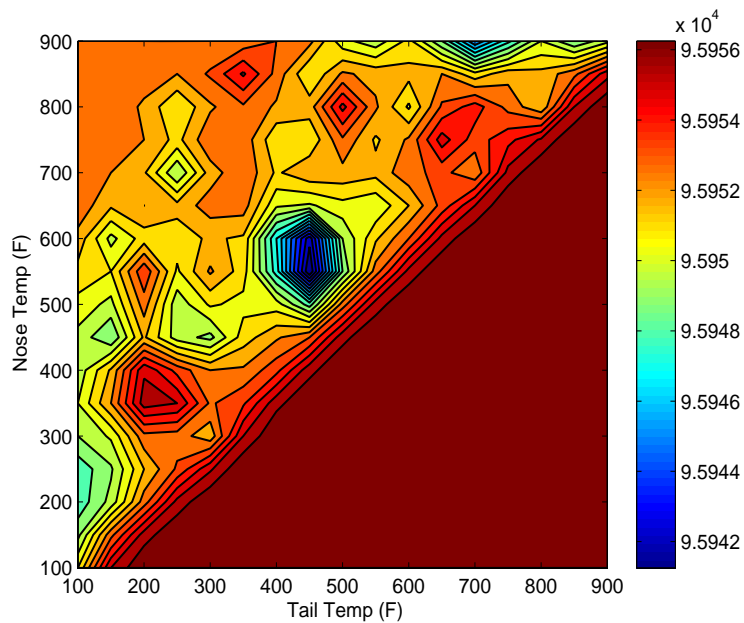
Figure 5-8: Control cost function Ω_{con} data (filtered) as a function of tail and nose temperature profiles.
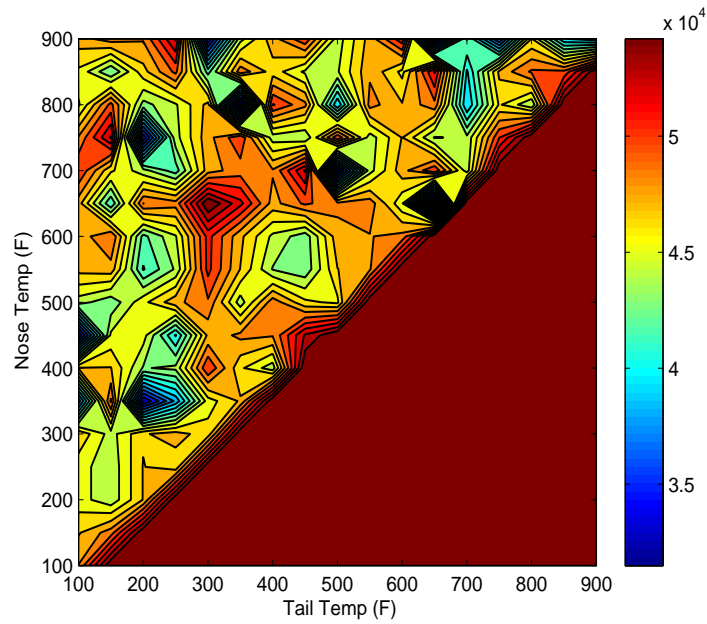
Figure 5-9: Error cost function Ω_{err} data as a function of tail and nose temperature profiles.
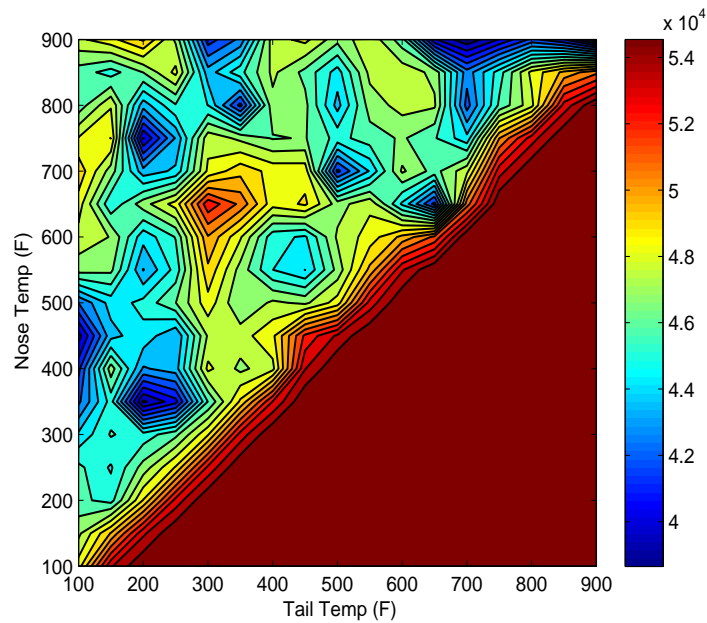
Figure 5-10: Error cost function Ω_{err} data (filtered) as a function of tail and nose temperature profiles.
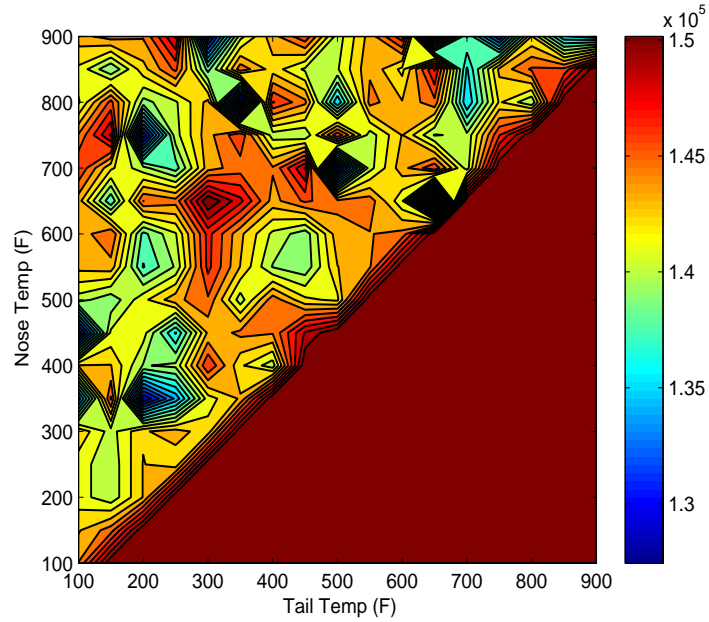
Figure 5-11: Total cost function Ω_{tot} data as a function of tail and nose temperature profiles.

sense, the total cost plots represent where the temperature parameters are best suited for control based on the given cost function. Since the cost of the control input is relatively constant, the total cost largely shows the same pattern as the error cost. In addition to the region between $T_{nose} \in [200, 600]^\circ F$ and $T_{tail} \in [100, 250]^\circ F$, there also seems to be a region between $T_{nose} = 900^\circ F$ and $T_{tail} \in [600, 900]^\circ F$, where the performance is also improved.

The control cost, error cost, and total cost were important in the optimization of the control gains and were used as the criteria for selecting which gain combination was considered near optimal. However, there are potentially other performance metrics of value. In addition to the optimization costs, the peak-to-peak transient errors, time to steady-state, and steady-state peak-to-peak errors were examined for further investigation. The peak-to-peak transient error is produced by taking the difference from the maximum and minimum transient tracking errors. The peak-to-peak error for the pitch rate $Q(t)$ is plotted in Figure 5-13 and Figure 5-14, and the peak-to-peak for the velocity $V(t)$ is

64
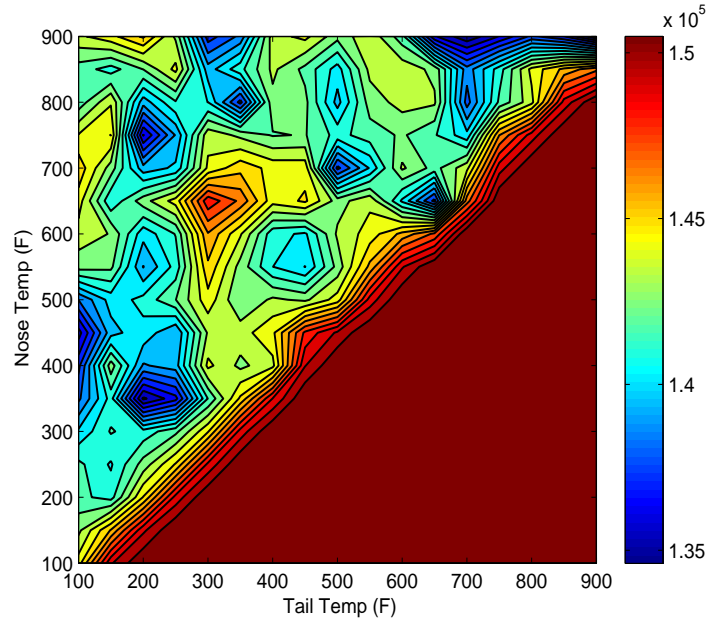
Figure 5-12: Total cost function Ω_{tot} data (filtered) as a function of tail and nose temperature profiles.

plotted in Figure 5-15 and Figure 5-16. The pitch rate peak-to-peak errors do not have a large variation for the different plants, other than a noticeable poor performing region around $T_{nose} = 550°F$ and $T_{tail} = 450°F$. The velocity peak-to-peak has a minimum around the similar $T_{nose} \in [200, 600]° F$ and $T_{tail} \in [100, 250]° F$. The velocity peak-to-peak has minimums when the pitch rate has maximums, indicating a degree of trade off between better velocity performance, but worse pitch rate performance, and vice versa.

An examination of the time to steady-state plots for pitch rate and velocity shown in Figures 5-17-5-20 indicates relatively similar transient times, with a few outliers. Having little variation means that all the plant models are similar in the transient times with this particular control design. The time to steady-state is calculated by looking at the transient performance and extracting the time it takes for the error signals to decay below the steady-state peak-to-peak error value.
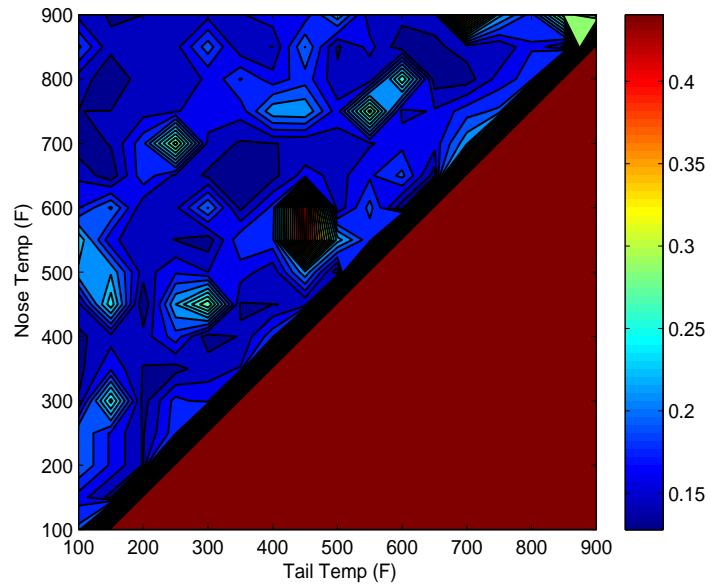
Figure 5-13: Peak-to-peak transient error for the pitch rate $Q(t)$ tracking error in deg./sec..
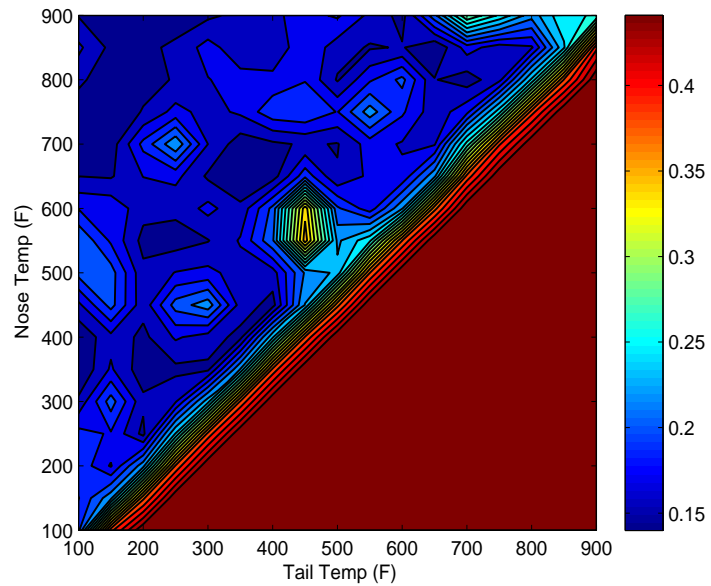
Figure 5-14: Peak-to-peak transient error (filtered) for the pitch rate $Q(t)$ tracking error in deg./sec..
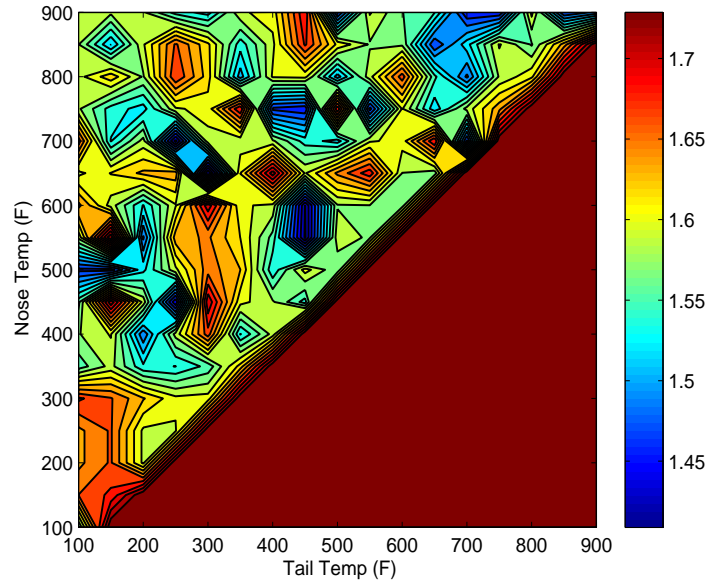
Figure 5-15: Peak-to-peak transient error for the velocity $V(t)$ tracking error in ft/sec..
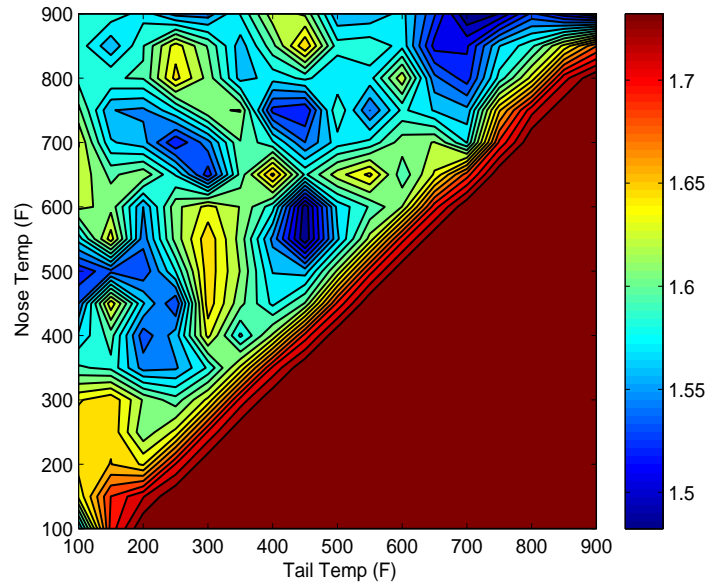
Figure 5-16: Peak-to-peak transient error (filtered) for the velocity $V(t)$ tracking error in ft./sec..
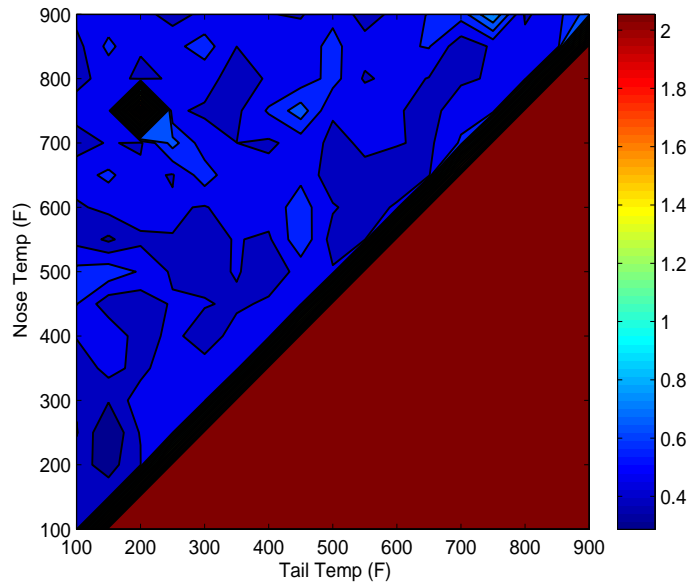
Figure 5-17: Time to steady-state for the pitch rate $Q(t)$ tracking error in seconds.
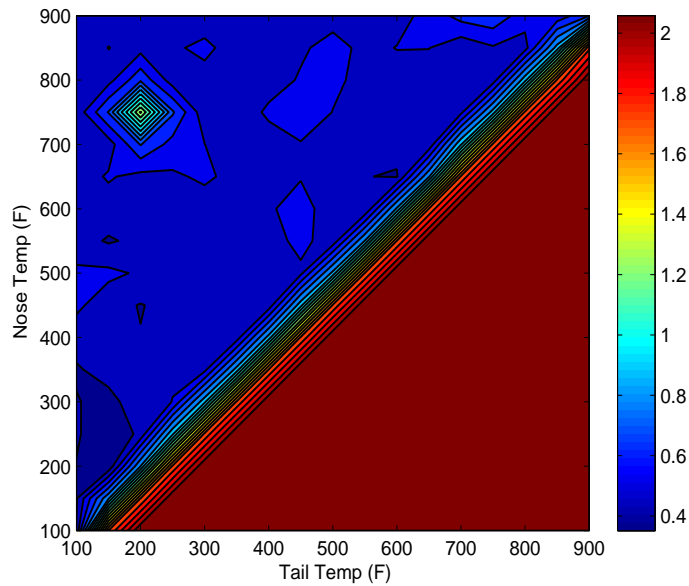
Figure 5-18: Time to steady-state (filtered) for the pitch rate $Q(t)$ tracking error in seconds.
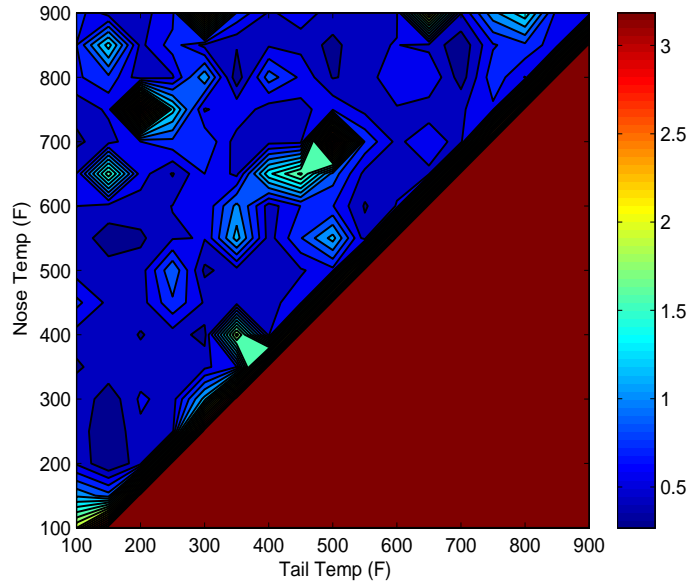
Figure 5-19: Time to steady-state for the velocity $V(t)$ tracking error in seconds.
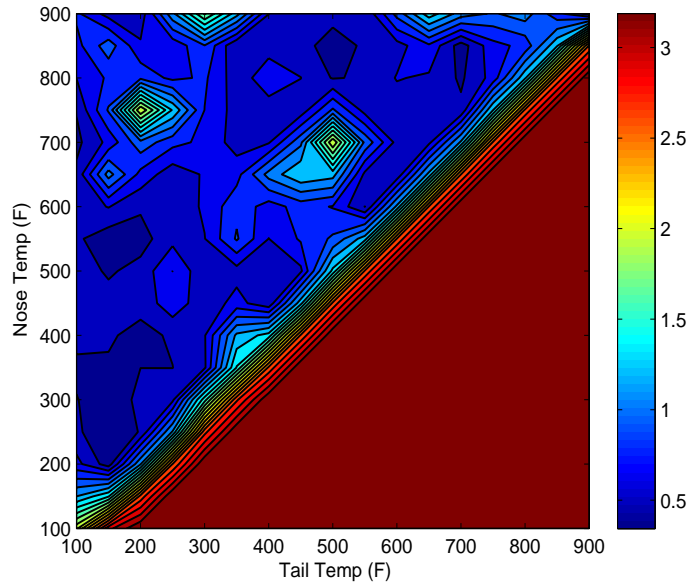
Figure 5-20: Time to steady-state (filtered) for the velocity $V(t)$ tracking error in seconds.
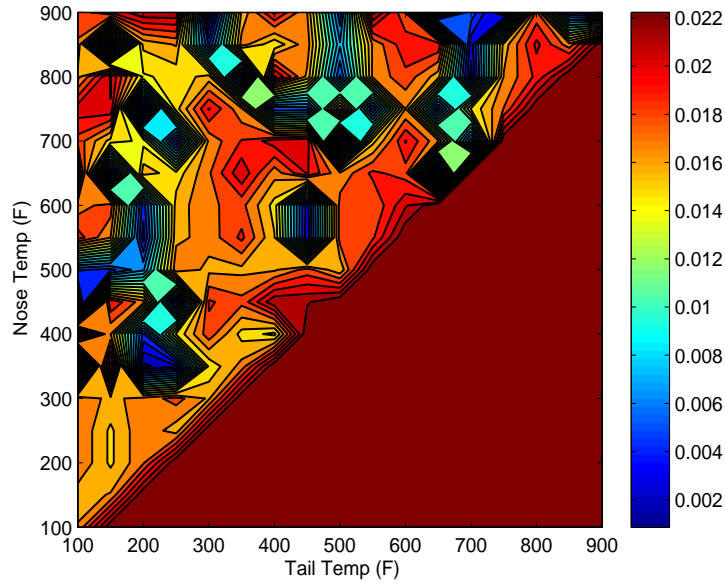
Figure 5-21: Steady-state peak-to-peak error for the pitch rate $Q(t)$ in deg./sec..

Finally, the steady-state peak-to-peak error values can be examined for both output signals. The steady-state peak-to-peak errors are calculated by waiting until the error signal falls to within some non-vanishing steady-state bound after the initial transients have died down, and then measuring the maximum peak-to-peak error within that bound. The plots for steady-state peak-to-peak error for the pitch rate and velocity are shown in Figures 5-21 - 5-24. The steady-state peak-to-peak errors show a minimum in the similar region as seen for other performance metrics, i.e. $T_{nose} \in [200, 600]^{\circ} F$ and $T_{tail} \in [100, 250]^{\circ} F$.

By normalizing all of the previous data about the minimum of each set of data, and then adding the plots together, a combined plot is obtained. This plot assumes that the designer weights each of the plots equally, but the method could be modified if certain aspects were deemed more important than others. Explicitly, data from each metric was combined as according to

$$\psi_{i,j} = \frac{1}{\lambda}\sum_{1}^{\lambda}\frac{\xi_{i,j}(\lambda)}{\min(\xi_{i,j}(\lambda))} \tag{5–8}$$

70
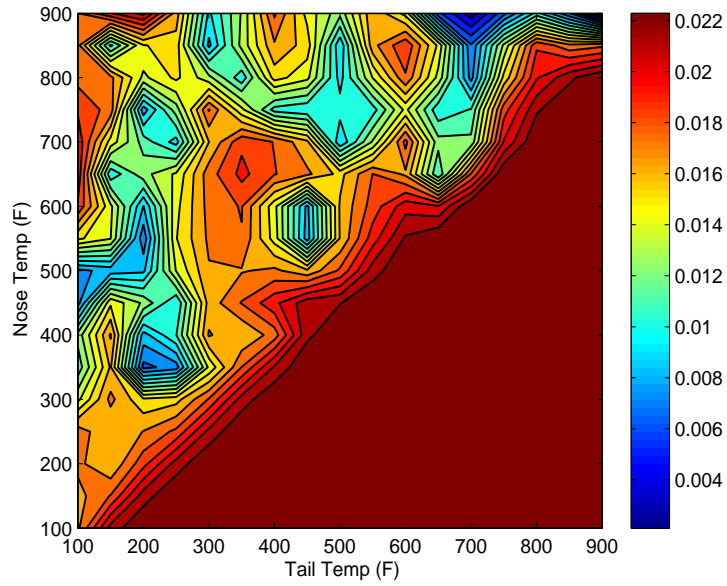
Figure 5-22: Steady-state peak-to-peak error (filtered) for the pitch rate $Q(t)$ in deg./sec..
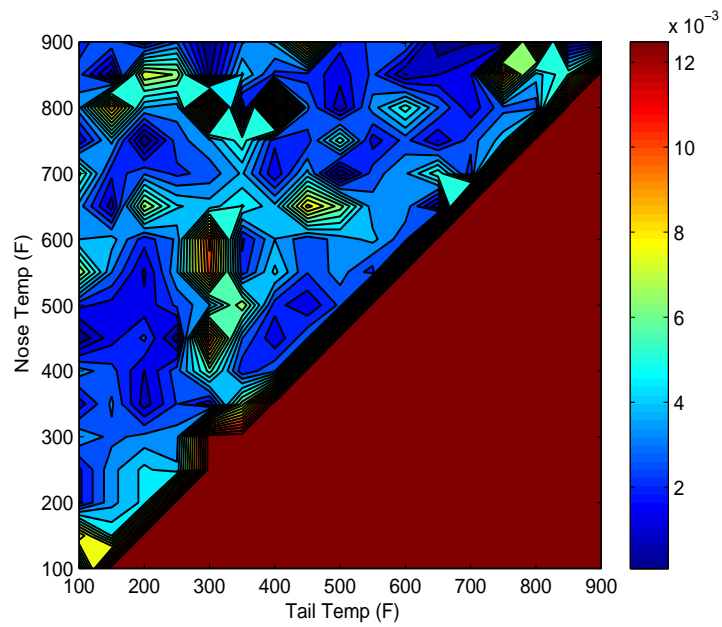
Figure 5-23: Steady-state peak-to-peak error for the velocity $V(t)$ in ft./sec..
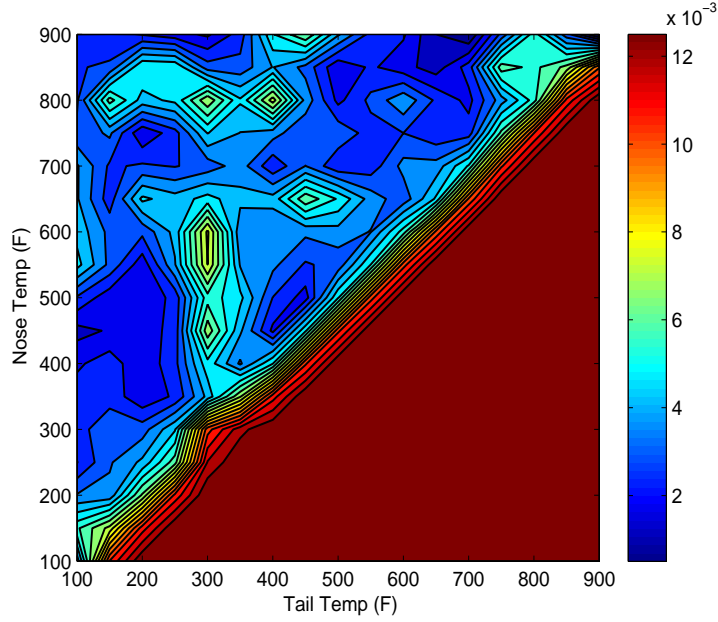
Figure 5-24: Steady-state peak-to-peak error (filtered) for the velocity $V(t)$ in ft./sec.

where ψ is the new combined and normalized temperature profile data, λ is the number of data sets being combined, and i, j are the location coordinates of the temperature data. Figure 5-25 shows this combination of control cost, error cost, peak-to-peak error, time to steady-state, and steady-state peak-to-peak error for both pitch rate and velocity tracking errors. By examining this cost function, an optimal region between $T_{nose} \in [200, 600]^\circ F$ and $T_{tail} \in [100, 250]^\circ F$ is determined.

In addition, optimal regions for the control gains can be examined. The control gains used for this problem are shown in (5–1) and (5–2) having the form

$$
\gamma = \begin{bmatrix} \gamma_1 & 0 \\ 0 & \gamma_2 \end{bmatrix}, \quad k_s = \begin{bmatrix} k_{s_1} & 0 \\ 0 & k_{s_2} \end{bmatrix}, \quad k_u = \begin{bmatrix} k_{u_1} & 0 \\ 0 & k_{u_2} \end{bmatrix}
$$

$$
k_\gamma = \begin{bmatrix} k_{\gamma_1} & 0 \\ 0 & k_{\gamma_2} \end{bmatrix}, \quad k_\Gamma = \begin{bmatrix} k_{\Gamma_1} & 0 \\ 0 & k_{\Gamma_2} \end{bmatrix}. \tag{5–9}
$$

By examining the control gains the maximum, minimum, mean, and standard deviation can be computed for all sets of control gains found to be near optimal. Table 5-1
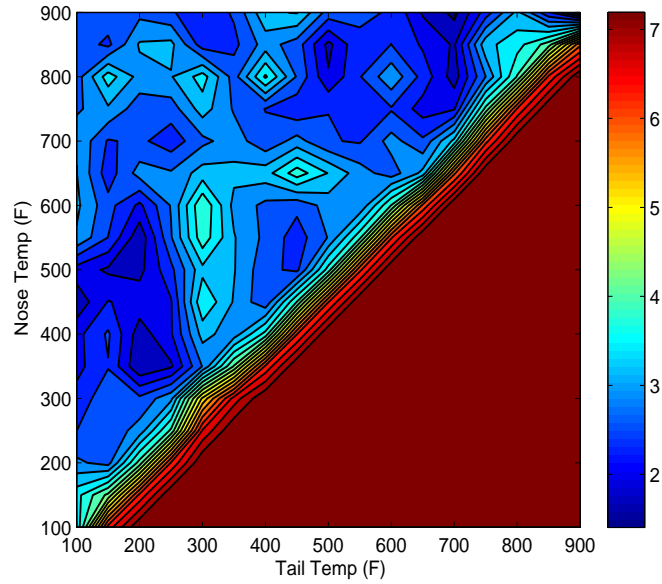
Figure 5-25: Combined optimization ψ chart of the control and error costs, transient and steady-state values.

Table 5-1: Optimization Control Gain Search Statistics

	γ_1	γ_2	k_{s_1}	k_{s_2}	k_{u_1}	k_{u_2}	k_{γ_1}	k_{γ_2}	k_{Γ_1}	k_{Γ_2}
Mean	25.35	36.60	16.07	265.3	28.38	9.65	27.43	14.12	0.972	0.8958
Std.	7.72	7.64	7.05	85.6	13.1	7.98	13.5	10.6	0.1565	0.133
Max	44.6	55.3	53.6	423.5	57.3	36.4	62.1	39.1	1.318	1.201
Min	7.14	3.58	6.30	9.762	0.360	0.050	0.392	0.110	0.658	0.6640

shows the control gain statistics. This data is useful in describing the optimal range for which control gains were selected. By knowing the region of near optimal attraction for the control gains, a future search could be confined to that region. The standard deviation also says something about the sensitivity of the control/aircraft dynamics, where larger standard deviations mean that particular gain has less effect on the overall system and vice a versa.

5.6   Conclusion

A control-oriented analysis of thermal gradients for a hypersonic vehicle (HSV) is presented. By incorporating nonlinear disturbances into the HSV model, a more representative control-oriented analysis can be performed. Using the nonlinear controller developed in Chapter 2 and Chapter 4, performance metrics were calculated for a number

of different HSV temperature profiles based on the design process initially developed in [6, 50]. Results from this analysis show that there is a range of temperature profiles that maximizes the controller effectiveness. For this particular study, the range was $T_{nose} \in [200, 600]^{\circ} F$ and $T_{tail} \in [100, 250]^{\circ} F$. In addition, this research has shown the range of control gains, useful for future design and numerical studies. This control-oriented analysis data is useful for HSV structural designs and thermal protection systems. Knowledge of a desirable temperature profile and control gains will allow engineers and designers to build a HSV with the proper thermal protection that will keep the vehicle within a desired operating range based on control performance. In addition, this numerical study provides information that can be further used in more elaborate analysis processes and demonstrates one possible method for obtaining performance data for a given controller on the complete nonlinear HSV model.

CHAPTER 6
CONCLUSIONS AND FUTURE WORK

6.1 Conclusions

A new type on controller is developed for LPV systems that robustly compensates for the unknown state matrix, disturbances, and compensates for the uncertainty in the input dynamic inversion. In comparison with previous results, this work presents a novel approach in control design that stands out from the classical gain scheduling techniques such as standard scheduling, the use of LMIs, and the more recent development of LFTs, including their non-convex μ-type optimization methods. Classical problems such as gain scheduling suffer from stability issues and the requirement that parameters only change slowly, limiting their use to quasi-linear cases. LMIs use convex optimization, but typically require the use of numerical optimization schemes and are analytically intractable except in rare cases. LFTs further the control design for LPV systems by using small gain theory, however they cannot deal explicitly with uncertain parameters. To handle uncertain parameters, the LFT problem is converted into a numerical optimization problem such as μ-type optimization. μ-type optimization is non-convex and therefore solutions may not be found even when they exist. The robust dynamic inversion control developed for uncertain LPV systems alleviates these problems. As long as some knowledge of the input matrix is known and certain invertability requirements are met then a stabilizing controller always exists. Proofs provided show that the controller is robust to disturbances, state dynamics, and uncertain parameters by using a new robust controller technique with exponential stability.

Common applications for LPV systems are flight controllers. This is because historically flight trajectories vary slowly with time and are well suited to the previously mentioned LPV control schemes such as gain scheduling. Recent advances in technology and aircraft design as well as more dynamic and demanding flight profiles have increased the demand on the controllers. In these demanding dynamic environments, parameters

no longer change slowly and may be unknown or uncertain. This renders previous control designs limiting. Motivated by this fact and specifically using the dynamics of an air-breathing HSV, the dynamics are shown to be modeled as an LPV system with uncertainties and disturbances. This work motivates the design and testing of the robust dynamic inversion controller on a temperature varying HSV. Using unknown temperature profiles, while simultaneously tracking an output trajectory, the robust controller is shown to compensate for unknown time-varying parameters in the presence of disturbances for the HSV. Using one set of control gains it was shown that stable control was maintained over the entire design space while performing maneuvers. Even though the control was developed for LPV systems, the simulation results are performed on the full nonlinear HSV flight and structural dynamics, hence validated the control-oriented modeling assumptions.

Finally, a numerical optimization scheme was performed on the same HSV model, using a combination of random search and evolving algorithms to produce dynamic optimization data for the combined vehicle and controller. Regions of optimality were shown to provide feedback to design engineers on the best suitable temperature profile parameter space. To remove ambiguity, the controller for each individual temperature profile case was optimally tuned and the tracking trajectory and disturbances were kept the same. Analytical methods do not exist for optimal gain tuning nonlinear controllers on nonlinear systems Hence, a numerical optimizing scheme was developed. By strategically searching the control gain space values were obtained, and the performance metrics at that point were compared across the vehicle design space. This work may be useful for future design problems for HSVs where the structural and dynamic design are performed in conjunction with the control design.

6.2   Contributions

- A new robust dynamic inversion controller was developed for general perturbed LPV systems. The control design requires knowledge of a best guess input matrix and at least as many inputs as tracked outputs. In the presence an unknown state matrix,

parameters, and disturbance, and with an uncertain input matrix, the developed
control design provides exponential tracking provided certain assumptions are met.
The developed control method takes a different approach to traditional LPV design
and provides a framework for future control design.

- Because the assumptions required of the controller are met by the HSV, a numerical
  simulation was performed. After reducing the HSV nonlinear dynamics to that
  of an LPV system motivation was provided to implement the controller designed.
  A simulation is provided where the full nonlinear HSV dynamics are used. The
  simulation demonstrates the efficacy of the proposed control design on this particular
  HSV application. A wide range of temperature variations were used and tracking
  control was implemented to demonstrate the performance of the controller.

- Further performance evaluation was conducted by designing an optimization proce-
  dure to analyze the interplay between the HSV dynamics, temperature parameters,
  and controller performance. A number of different temperature plant models for
  HSV were near optimally tuned using a combination of a random search and evolv-
  ing algorithms. Next, the control performance was evaluated and compared to the
  other HSV temperature models. Comparative analysis is provided that suggests
  regions where the temperature profiles of the HSV in conjunction with the proposed
  control design achieve improved performance results. These results may provide
  insight to structural systems designers for HSVs as well as provide scaffolding for
  future numerical design optimization and control tuning.

6.3   Future Work

- The robust dynamic inversion control design in this dissertation requires knowledge
  of the sign of the error signal derivative terms. While these measurements may be
  available for specific applications, this underlying necessity reduces the generality of
  the controller. Future work could focus on removing this restriction, and producing
  an output feedback only robust dynamic inversion control.

- Another requirement of the control design is the requirement of the diagonal dominance of the best guess feed forward input matrix. While this requirement is not unreasonable because it only requires that the guess be within the vicinity of the actual value, future work could focus on relaxing that requirement. Alleviating this restriction could potentially be done by using partial adaptation laws while simultaneously using robust algorithms to counter the parameter variations.

- It was shown that the controller developed is able to track inner-loop states for the HSV, however it would be beneficial to adapt this inner loop control design to an outer loop flight planning controller. In this way, more practical planned trajectories can be tracked (e.g., altitude) by using the inner loop of pitch rate and pitch angle control. Additionally, this same result can be attained by using backstepping techniques. By backstepping through other state dynamics (e.g., altitude) and into the control dynamics (e.g., pitch rate), a combined controller could be developed.

- The temperature and control gain optimization provides a good framework for finding HSV designs with increased performance. It would be interesting in future work to re-analyze the optimal control gain space, and see if it could be converged to a smaller set. If the optimal set could be further converged, then through numerous iterations a very precise and narrow range may be found. Finding a more optimal design space may aid in future structural optimization searches.

- It would also be beneficial for the optimization work to have more accurate nonlinear models. Obtaining better models will require working in collusion with HSV designers. Getting high quality feedback on the design constraints and flight trajectory constraints would further aid the search for optimality in regards to control gains and temperature profiles. In addition, the dynamics could be modeled and simulated with higher certainty if more details were known. Combining extra data on the dynamics into the control design would help further the development of actual flight worthy vehicles.

APPENDIX A
OPTIMIZATION DATA

The data presented in the following tables is the raw data from the images presented in Chapter 5. The rows contains all of the T_{nose} in $^\circ F$ and the columns contain the T_{tail} in $^\circ F$. Empty spaces are places where the tail temperature is higher than the nose temperature, and are outside the design space of this work and ommitted.

Table A-1: Total cost function, used to generate Figure 5-11 and 5-12 (Part 1)

T_{nose} °F	T_{tail}°F								
	100	150	200	250	300	350	400	450	500
100	144526								
150	143210	145071							
200	141588	140254	143397						
250	141588	140254	143397	142557					
300	143086	140577	143199	143895	142656				
350	133478	145807	129636	134531	141681	143496			
400	143490	143396	139825	140233	146708	142439	140353		
450	129673	141283	141577	136368	143591	144789	144610	149182	
500	140466	139064	141863	144110	145435	140439	145178	142468	141932
550	143730	144033	137552	140079	147113	143303	139847	139083	143308
600	143730	145599	138430	140945	147159	143625	140785	139202	144040
650	143884	137784	145621	144958	151291	148236	144025	145853	144782
700	146708	142439	140353	138181	143955	145086	144610	149182	129812
750	144610	149182	129812	140633	144027	146527	140466	139965	146527
800	140845	146015	139499	140904	143730	129426	146864	144790	135440
850	141959	138801	142931	145923	138328	145212	142817	140848	140940
900	143955	145086	144610	149182	129812	140633	144027	146527	140466

Table A-2: Total cost function, used to generate Figure 5-11 and 5-12 (Part 2)

T_{nose} °F	T_{tail}°F							
	550	600	650	700	750	800	850	900
550	144322							
600	144420	144857						
650	145109	141262	127435					
700	140633	144027	146527	140466				
750	140466	143396	139825	140233	146708			
800	144948	143418	145297	135394	142384	140069		
850	144253	141883	148014	136336	143641	145803	145941	
900	143828	147566	129349	138888	131875	142296	135461	134603

Table A-3: Control input cost function, used to generate Figure 5-7 and 5-8 (Part 1)

T_{nose} °F	T_{tail}°F								
	100	150	200	250	300	350	400	450	500
100	95951								
150	95949	95953							
200	95948	95949	95952						
250	95948	95949	95952	95952					
300	95949	95950	95953	95953	95949				
350	95952	95952	95957	95957	95953	95953			
400	95948	95953	95957	95953	95954	95952	95953		
450	95951	95946	95952	95950	95946	95953	95952	95953	
500	95950	95950	95954	95948	95953	95949	95952	95948	95953
550	95952	95950	95957	95949	95954	95952	95948	95937	95949
600	95952	95949	95950	95952	95951	95952	95948	95937	95952
650	95953	95952	95953	95953	95953	95954	95949	95953	95950
700	95954	95952	95953	95946	95953	95953	95952	95953	95952
750	95952	95953	95952	95953	95953	95954	95950	95950	95954
800	95953	95953	95953	95949	95953	95952	95953	95952	95957
850	95952	95953	95953	95953	95953	95957	95953	95949	95953
900	95953	95953	95952	95953	95952	95953	95953	95954	95950

Table A-4: Control input cost function, used to generate Figure 5-7 and 5-8 (Part 2)

T_{nose} °F	T_{tail}°F							
	550	600	650	700	750	800	850	900
550	95952							
600	95952	95952						
650	95949	95952	95952					
700	95953	95953	95954	95950				
750	95950	95953	95957	95953	95954			
800	95953	95949	95953	95949	95953	95949		
850	95953	95952	95953	95952	95953	95952	95953	
900	95948	95953	95951	95940	95949	95953	95946	95950

Table A-5: Error cost function, used to generate Figure 5-9 and 5-10 (Part 1)

T_{nose} °F	T_{tail}°F								
	100	150	200	250	300	350	400	450	500
100	48574								
150	47260	49118							
200	45639	44304	47444						
250	45639	44304	47444	46605					
300	47136	44626	47245	47942	46706				
350	37525	49855	33679	38574	45727	47542			
400	47541	47443	43867	44280	50754	46487	44400		
450	33721	45337	45625	40418	47644	48835	48658	53228	
500	44516	43114	45908	48162	49482	44490	49225	46519	45979
550	47777	48082	41594	44129	51159	47350	43898	43146	47358
600	47857	49649	42479	44992	51208	47673	44837	43264	48088
650	47930	41831	49667	49005	55337	52281	48075	49900	48831
700	50754	46487	44400	42235	48002	49133	48658	53228	33860
750	48658	53228	33860	44680	48074	50572	44516	44015	50572
800	44892	50062	43546	44954	47776	33474	50911	48837	39482
850	46007	42848	46978	49969	42375	49254	46864	44898	44986
900	48002	49133	48658	53228	33860	44680	48074	50572	44516

Table A-6: Error cost function, used to generate Figure 5-9 and 5-10 (Part 2)

T_{nose} °F	T_{tail}°F							
	550	600	650	700	750	800	850	900
550	48370							
600	48467	48905						
650	49160	45310	31482					
700	44680	48074	50572	44516				
750	44516	47443	43867	44280	50754			
800	48995	47469	49343	39438	46430	44120		
850	48299	45931	52060	40384	47688	49850	49987	
900	47880	51613	33397	42947	35925	46342	39514	38653

Table A-7: Pitch rate, peak-to-peak error, used to generate Figure 5-13 and 5-14 (Part 1)

T_{nose} °F	T_{tail}°F								
	100	150	200	250	300	350	400	450	500
100	0.1951								
150	0.1678	0.1377							
200	0.2057	0.1722	0.1421						
250	0.2057	0.1722	0.1421	0.1842					
300	0.1450	0.2588	0.1365	0.1803	0.1669				
350	0.1374	0.1712	0.1427	0.1372	0.1536	0.1601			
400	0.1399	0.1530	0.1500	0.1835	0.1336	0.1448	0.1849		
450	0.1535	0.2478	0.1278	0.2214	0.2839	0.1421	0.1434	0.1436	
500	0.2175	0.2197	0.1505	0.1728	0.1590	0.1672	0.1481	0.2174	0.1292
550	0.2338	0.1624	0.1491	0.1430	0.1343	0.1867	0.1848	0.4458	0.2287
600	0.1738	0.2085	0.1465	0.1548	0.2071	0.1394	0.1799	0.4561	0.1471
650	0.1560	0.1327	0.1857	0.1553	0.1406	0.1400	0.1374	0.1665	0.1530
700	0.1336	0.1448	0.1849	0.2928	0.1539	0.1415	0.1434	0.1436	0.1530
750	0.1434	0.1436	0.1530	0.1573	0.1692	0.1655	0.2175	0.2200	0.1655
800	0.1510	0.1331	0.1502	0.1573	0.1595	0.1916	0.1655	0.1832	0.1473
850	0.1939	0.1468	0.1532	0.1532	0.1992	0.1464	0.1432	0.2064	0.1409
900	0.1539	0.1415	0.1434	0.1436	0.1530	0.1573	0.1688	0.1655	0.2175

Table A-8: Pitch rate, peak-to-peak error, used to generate Figure 5-13 and 5-14 (Part 2)

T_{nose} °F	T_{tail}°F							
	550	600	650	700	750	800	850	900
550	0.1787							
600	0.1960	0.1309						
650	0.1719	0.1947	0.1353					
700	0.1573	0.1692	0.1655	0.2175				
750	0.2912	0.1530	0.1612	0.1835	0.1939			
800	0.1471	0.2673	0.1356	0.1354	0.1658	0.1833		
850	0.1641	0.1323	0.1398	0.1507	0.1438	0.1733	0.1395	
900	0.1491	0.1493	0.1499	0.3929	0.2276	0.1822	0.2941	0.2615

Table A-9: Pitch rate, steady-state peak-to-peak error, used to generate Figure 5-21 and 5-22 (Part 1)

T_{nose} °F	T_{tail} °F								
	100	150	200	250	300	350	400	450	500
100	0.0170								
150	0.0163	0.0170							
200	0.0179	0.0156	0.0178						
250	0.0179	0.0156	0.0178	0.0163					
300	0.0176	0.0166	0.0173	0.0184	0.0167				
350	0.0027	0.0233	0.0016	0.0028	0.0150	0.0173			
400	0.0232	0.0169	0.0048	0.0149	0.0186	0.0154	0.0144		
450	0.0012	0.0200	0.0173	0.0031	0.0192	0.0183	0.0221	0.0221	
500	0.0053	0.0048	0.0070	0.0177	0.0166	0.0166	0.0167	0.0184	0.0160
550	0.0196	0.0169	0.0036	0.0166	0.0173	0.0193	0.0159	0.0032	0.0185
600	0.0173	0.0186	0.0045	0.0163	0.0178	0.0183	0.0154	0.0034	0.0185
650	0.0222	0.0027	0.0164	0.0152	0.0178	0.0210	0.0173	0.0202	0.0171
700	0.0186	0.0154	0.0144	0.0039	0.0172	0.0191	0.0207	0.0211	0.0008
750	0.0207	0.0211	0.0008	0.0154	0.0202	0.0171	0.0053	0.0056	0.0171
800	0.0165	0.0213	0.0146	0.0151	0.0163	0.0029	0.0214	0.0166	0.0050
850	0.0179	0.0030	0.0161	0.0170	0.0049	0.0174	0.0150	0.0176	0.0074
900	0.0182	0.0202	0.0221	0.0221	0.0008	0.0160	0.0204	0.0169	0.0053

Table A-10: Pitch rate, steady-state peak-to-peak error, used to generate Figure 5-21 and 5-22 (Part 2)

T_{nose} °F	T_{tail} °F							
	550	600	650	700	750	800	850	900
550	0.0188							
600	0.0180	0.0210						
650	0.0193	0.0185	0.0019					
700	0.0154	0.0202	0.0171	0.0053				
750	0.0048	0.0169	0.0046	0.0149	0.0180			
800	0.0171	0.0187	0.0163	0.0026	0.0170	0.0193		
850	0.0171	0.0198	0.0199	0.0034	0.0163	0.0204	0.0173	
900	0.0226	0.0179	0.0009	0.0058	0.0015	0.0183	0.0041	0.0021

Table A-11: Pitch rate, time to steady-state, used to generate Figure 5-17 and 5-18 (Part 1)

T_{nose} $^\circ F$	$T_{tail}^\circ F$								
	100	150	200	250	300	350	400	450	500
100	0.439								
150	0.429	0.433							
200	0.412	0.338	0.451						
250	0.471	0.287	0.472	0.541					
300	0.450	0.381	0.518	0.518	0.515				
350	0.394	0.499	0.431	0.540	0.512	0.472			
400	0.471	0.542	0.412	0.494	0.402	0.511	0.474		
450	0.556	0.407	0.405	0.475	0.473	0.444	0.482	0.519	
500	0.580	0.613	0.542	0.450	0.424	0.473	0.404	0.496	0.473
550	0.436	0.358	0.444	0.461	0.442	0.468	0.450	0.618	0.427
600	0.447	0.493	0.518	0.475	0.457	0.513	0.506	0.593	0.473
650	0.518	0.570	0.489	0.457	0.601	0.475	0.495	0.533	0.408
700	0.425	0.471	0.449	0.677	0.497	0.464	0.449	0.496	0.450
750	0.497	0.496	2.143	0.474	0.453	0.445	0.564	0.692	0.470
800	0.442	0.491	0.450	0.471	0.494	0.426	0.473	0.495	0.587
850	0.432	0.576	0.470	0.527	0.593	0.464	0.477	0.517	0.572
900	0.494	0.492	0.497	0.427	0.486	0.496	0.467	0.455	0.537

Table A-12: Pitch rate, time to steady-state, used to generate Figure 5-17 and 5-18 (Part 2)

T_{nose} $^\circ F$	$T_{tail}^\circ F$							
	550	600	650	700	750	800	850	900
550	0.450							
600	0.421	0.476						
650	0.453	0.403	0.423					
700	0.472	0.471	0.445	0.564				
750	0.548	0.473	0.430	0.518	0.479			
800	0.451	0.495	0.460	0.449	0.474	0.522		
850	0.503	0.537	0.558	0.404	0.478	0.495	0.469	
900	0.421	0.491	0.559	0.592	0.818	0.449	0.521	0.692

Table A-13: Velocity, peak-to-peak error, used to generate Figure 5-15 and 5-16 (Part 1)

T_{nose} °F	T_{tail}°F								
	100	150	200	250	300	350	400	450	500
100	1.5670								
150	1.6649	1.6847							
200	1.6446	1.6669	1.5972						
250	1.6445	1.6668	1.5973	1.5986					
300	1.6839	1.6663	1.6344	1.6055	1.6081				
350	1.5596	1.5904	1.5401	1.5366	1.5580	1.6235			
400	1.5836	1.6022	1.4917	1.5910	1.6735	1.5357	1.5910		
450	1.5634	1.7254	1.5946	1.4420	1.7098	1.6064	1.5872	1.5456	
500	1.4686	1.4651	1.5321	1.5966	1.6579	1.6329	1.5408	1.6075	1.5710
550	1.5893	1.7447	1.4859	1.6417	1.6516	1.6166	1.5627	1.4219	1.5953
600	1.6537	1.5934	1.5359	1.5993	1.7076	1.6038	1.5962	1.4238	1.5834
650	1.5961	1.6176	1.6366	1.6426	1.4089	1.6170	1.7221	1.5990	1.6525
700	1.6735	1.5357	1.5910	1.4344	1.5949	1.5890	1.5876	1.5456	1.5294
750	1.5876	1.5456	1.5294	1.5980	1.6078	1.6965	1.4686	1.4606	1.6965
800	1.5948	1.6270	1.5828	1.6800	1.6248	1.5124	1.6033	1.6058	1.5128
850	1.5855	1.5205	1.5984	1.6675	1.6205	1.5433	1.5966	1.6834	1.6128
900	1.5940	1.5890	1.5872	1.5456	1.5294	1.5980	1.6078	1.6965	1.4686

Table A-14: Velocity, peak-to-peak error, used to generate Figure 5-15 and 5-16 (Part 2)

T_{nose} °F	T_{tail}°F							
	550	600	650	700	750	800	850	900
550	1.5814							
600	1.5843	1.5756						
650	1.6916	1.5845	1.5754					
700	1.5980	1.6078	1.6965	1.4686				
750	1.4662	1.6022	1.5254	1.5910	1.6436			
800	1.5951	1.6737	1.5572	1.4852	1.5873	1.6127		
850	1.5830	1.5817	1.4735	1.5305	1.6027	1.5670	1.6405	
900	1.6025	1.5693	1.5542	1.4585	1.4581	1.6060	1.4721	1.4935

Table A-15: Velocity, steady-state peak-to-peak, used to generate Figure 5-23 and 5-24 (Part 1)

T_{nose} °F	T_{tail}°F								
	100	150	200	250	300	350	400	450	500
100	0.0037								
150	0.0088	0.0050							
200	0.0018	0.0036	0.0046						
250	0.0019	0.0038	0.0047	0.0039					
300	0.0037	0.0030	0.0034	0.0035	0.0131				
350	0.0016	0.0033	0.0010	0.0026	0.0015	0.0066			
400	0.0035	0.0028	0.0013	0.0029	0.0059	0.0021	0.0031		
450	0.0002	0.0017	0.0027	0.0004	0.0105	0.0032	0.0014	0.0031	
500	0.0021	0.0017	0.0015	0.0027	0.0037	0.0069	0.0022	0.0014	0.0027
550	0.0069	0.0032	0.0012	0.0037	0.0103	0.0022	0.0046	0.0026	0.0035
600	0.0038	0.0041	0.0022	0.0033	0.0108	0.0018	0.0038	0.0027	0.0035
650	0.0035	0.0010	0.0070	0.0045	0.0041	0.0051	0.0040	0.0084	0.0066
700	0.0059	0.0021	0.0031	0.0024	0.0028	0.0039	0.0014	0.0040	0.0008
750	0.0014	0.0040	0.0008	0.0029	0.0037	0.0055	0.0021	0.0022	0.0055
800	0.0035	0.0094	0.0038	0.0034	0.0118	0.0009	0.0126	0.0033	0.0008
850	0.0028	0.0003	0.0075	0.0068	0.0006	0.0045	0.0024	0.0023	0.0016
900	0.0023	0.0031	0.0031	0.0008	0.0031	0.0040	0.0099	0.0021	0.0027

Table A-16: Velocity, steady-state peak-to-peak, used to generate Figure 5-23 and 5-24 (Part 2)

T_{nose} °F	T_{tail}°F							
	550	600	650	700	750	800	850	900
550	0.0022							
600	0.0040	0.0027						
650	0.0034	0.0036	0.0008					
700	0.0029	0.0037	0.0055	0.0021				
750	0.0016	0.0028	0.0013	0.0029	0.0041			
800	0.0035	0.0054	0.0032	0.0015	0.0030	0.0028		
850	0.0027	0.0007	0.0013	0.0018	0.0101	0.0041	0.0057	
900	0.0027	0.0033	0.0002	0.0006	0.0005	0.0107	0.0005	0.0009

Table A-17: Velocity, time to steady-state, used to generate Figure 5-19 and 5-20 (Part 1)

T_{nose} $^\circ F$	$T_{tail}^\circ F$								
	100	150	200	250	300	350	400	450	500
100	2.012								
150	1.119	0.915							
200	0.539	0.268	0.496						
250	0.498	0.284	0.528	0.506					
300	0.543	0.314	0.586	0.492	1.201				
350	0.383	0.520	0.474	0.472	0.522	0.701			
400	0.501	0.515	0.403	0.492	0.355	1.94	0.516		
450	0.747	0.521	0.491	0.821	0.543	0.491	0.513	0.637	
500	0.494	0.472	0.484	0.983	0.378	0.502	0.481	0.542	0.656
550	0.492	0.339	0.385	0.546	0.568	1.208	0.496	0.841	1.201
600	0.562	0.500	0.493	0.563	0.578	1.043	0.492	0.708	0.712
650	0.562	1.681	0.627	0.400	0.705	0.521	1.396	1.760	0.932
700	0.383	0.498	0.704	0.808	0.836	0.491	0.504	0.516	3.330
750	0.459	0.587	3.300	1.347	0.539	0.679	0.473	0.496	0.680
800	0.678	0.817	0.459	0.538	1.114	0.309	0.929	0.675	0.403
850	0.702	1.356	0.522	0.776	0.514	0.430	0.541	0.511	0.363
900	0.798	0.480	0.519	0.632	2.844	0.822	0.543	0.607	0.518

Table A-18: Velocity, time to steady-state, used to generate Figure 5-19 and 5-20 (Part 2)

T_{nose} $^\circ F$	$T_{tail}^\circ F$							
	550	600	650	700	750	800	850	900
550	0.473							
600	0.398	0.568						
650	0.515	0.516	0.519					
700	0.821	0.520	0.679	0.473				
750	0.518	0.541	0.473	0.541	0.671			
800	0.467	0.705	0.702	0.337	0.802	0.550		
850	0.542	0.564	0.518	0.300	0.688	0.818	0.607	
900	0.474	0.545	2.293	0.564	1.095	1.393	0.642	0.559

REFERENCES

[1] L. K. Abbasa, C. Qian, P. Marzocca, G. Zafer, and A. Mostafa, "Active aerother-moelastic control of hypersonic double-wedge lifting surface," *Chin. J. Aeronaut.*, vol. 21, pp. 8–18, 2008.

[2] P. Apkarian and P. Gahinet, "A convex characterisation of gain-scheduled h-inf controllers," *IEEE Transactions on Automatic Control*, vol. 40, pp. 853–864, 1995.

[3] P. Apkarian and H. D. Tuan, "Parameterized lmis in control theory," *SIAM J. Contr. Optim.*, vol. 38, no. 4, pp. 1241–1264, 2000.

[4] K. J. Austin and P. A. Jacobs, "Application of genetic algorithms to hypersonic flight control," in *IFSA World Congr., NAFIPS Int. Conf.*, Vancouver, British Columbia, Canada, July 2001, pp. 2428–2433.

[5] G. J. Balas, "Linear parameter varying control and its application to a turbofan engine," *Int. J. Non-linear and Robust Control, Special issue on Gain Scheduled Control*, vol. 12, no. 9, pp. 763–798, 2002.

[6] S. Bhat and R. Lind, "Control-oriented analysis of thermal gradients for a hypersonic vehicle," in *Proc. IEEE Am. Control Conf.*, 2009.

[7] J. M. Biannie and P. Apkarian, "Missile autopilot design via a modified lpv synthesis technique," *Aerosp. Sci. Technol.*, pp. 763–798, 1999.

[8] M. Bolender and D. Doman, "A non-linear model for the longitudinal dynamics of a hypersonic air-breathing vehicle," in *Proc. AIAA Guid. Navig. Control Conf.*, San Francisco, CA, Aug. 2005.

[9] ——, "Modeling unsteady heating effects on the strucutral dynamics of a hypersonic vehicle," in *AIAA Atmos. Flight Mech. Conf.*, Keystone, CO, Aug. 2006.

[10] M. A. Bolender and D. B. Doman, "Nonlinear longitudinal dynamical model of an air-breathing hypersonic vehicle," *J. Spacecraft Rockets*, vol. 44, no. 2, pp. 374–387, Apr. 2007.

[11] S. Boyd, L. E. Ghaoui, E. Feron, and V. Balakrishnan, *Linear matrix inequalities in system and control theory.* SIAM, 1994.

[12] A. J. Culler, T. Williams, and M. A. Bolender, "Aerothermal modeling and dynamic analysis of a hypersonic vehicle," in *AIAA Atmos. Flight Mech. Conf.*, Hilton Head, SC, Aug. 2007.

[13] J. Daafouz, J. Bernussou, and J. C. Geromel, "On inexact lpv control design of continuous-time polytopic systems," *IEEE Transactions on Automatic Control*, vol. Vol. 53, No. 7, no. 7, August 2008.

[14] M. Dinh, G. Scorletti, V. Fromion, and E. Magarotto, "Parameter dependent h-inf control by finite dimensional lmi optimization: application to trade-off dependent control," *Int. J. Robust Nonlinear Contr.*, vol. 15, no. 9, pp. 383–406, 2005.

[15] A. Filippov, *Differential equations with discontinuous right-hand side*. Netherlands: Kluwer Academic Publishers, 1988.

[16] L. Fiorentini, A. Serrani, M. A. Bolender, and D. B. Doman, "Nonlinear robust/adaptive controller design for an air-breathing hypersonic vehicle model," in *Proc. AIAA Guid. Navig. Control Conf.*, Hilton Head, SC, Aug. 2007.

[17] ——, "Nonlinear robust adaptive control of flexible air-breathing hypersonic vehicle," *J. Guid. Contr. Dynam.*, vol. 32, No. 2, pp. 402–417, April 2009.

[18] P. Gaspa, I. Szaszi, and J. Bokor, "Active suspension design using linear parameter varying control," *Int. J. Vehicle Auton. Syst.*, vol. 1, no. 2, pp. 206–221, 2003.

[19] T. Gibson, L. Crespo, and A. Annaswamy, "Adaptive control of hypersonic vehicles in the presence of modeling uncertainties," in *Proc. IEEE Am. Control Conf.*, June 2009.

[20] S. Gutman, "Uncertain dynamical systems–a Lyapunov min-max approach," *IEEE Trans. Autom. Control*, vol. 24, no. 3, pp. 437–443, 1979.

[21] J. Heeg, T. A. Zeiler, A. S. Pototzky, and C. V. Spain, "Aerothermoelastic analysis of a NASP demonstrator model," in *Proc. of the AIAA Structures Struct. Dyn. Mater. Conf.*, La Jolla, CA, Apr. 1993.

[22] A. Helmersson, "mu synthesis and lft scheduling with mixed uncertainties," in *Proceedings of the European Control Conference*, 1995, pp. 153–158.

[23] P. Jankovsky, D. O. Sigthorsson, A. Serrani, and S. Yurkovich, "Output feedback control and sensor placement for a hypersonic vehicle model," in *Proc. AIAA Guid. Navig. Control Conf.*, Hilton Head, SC, Aug. 2007.

[24] N. J. Killingsworth and M. Krstic, "PID tuning using extremum seeking: online, model-free performance optimization," *IEEE Contr. Syst. Mag.*, vol. 26, no. 1, pp. 70–79, 2006.

[25] L. Li and V. A. Ugrinovshii, "Robust stabilization of lpv systems with structured uncertainty using minimax controllers," in *IEEE Conference on Decision and Control*, 2007.

[26] R. Lind, "Linear parameter-varying modeling and control of structural dynamics with aerothermoelastic effects," *J. Guid. Contr. Dynam.*, vol. 25, no. 4, pp. 733–739, July-Aug. 2002.

[27] W. MacKunis, K. Kaiser, Z. D. Wilcox, and W. E. Dixon, "Global adaptive output feedback tracking control of an unmanned aerial vehicle," *IEEE Trans. Control Syst. Technol.*, to appear, 2010.

[28] W. MacKunis, M. K. Kaiser, P. M. Patre, and W. E. Dixon, "Adaptive dynamic inversion for asymptotic tracking of an aircraft reference model," in *Proc. AIAA Guid. Navig. Control Conf.*, Honolulu, HI, 2008.

[29] W. MacKunis, Z. D. Wilcox, K. Kaiser, and W. E. Dixon, "Global adaptive output feedback MRAC," in *Proc. IEEE Conf. Decis. Control Chin. Control Conf.*, 2009.

[30] C. I. Marrison and R. F. Stengel, "Design of robust control systems for a hypersonic aircraft," *J. Guid. Contr. Dynam.*, vol. 21, no. 1, pp. 58–63, 1998.

[31] A. Packard, "Gain scheduling via linear fractional transformations," *Systems & Control Letters*, vol. 22, no. 2, pp. 79–92, 1994.

[32] J. T. Parker, A. Serrani, S. Yurkovich, M. A. Bolender, and D. B. Doman, "Control-oriented modeling of an air-breathing hypersonic vehicle," *J. Guid. Contr. Dynam.*, vol. 30, no. 3, pp. 856–869, 2007.

[33] P. Patre, W. Mackunis, M. Johnson, and W. Dixon, "Composite adaptive control for Euler-Lagrange systems with additive disturbances," *Automatica*, vol. 46, no. 1, pp. 140–147, 2010.

[34] P. M. Patre, K. Dupree, W. MacKunis, and W. E. Dixon, "A new class of modular adaptive controllers, part II: Neural network extension for non-LP systems," in *Proc. IEEE Am. Control Conf.*, 2008, pp. 1214–1219.

[35] P. M. Patre, W. MacKunis, K. Dupree, and W. E. Dixon, "A new class of modular adaptive controllers, part I: Systems with linear-in-the-parameters uncertainty," in *Proc. IEEE Am. Control Conf.*, 2008, pp. 1208–1213.

[36] ——, *RISE-Based Robust and Adaptive Control of Nonlinear Systems*. Boston: Birkhäuser, 2009, under contract.

[37] P. M. Patre, W. MacKunis, K. Kaiser, and W. E. Dixon, "Asymptotic tracking for uncertain dynamic systems via a multilayer neural network feedforward and RISE feedback control structure," *IEEE Trans. Autom. Control*, vol. 53, no. 9, pp. 2180–2185, 2008.

[38] P. M. Patre, W. Mackunis, C. Makkar, and W. E. Dixon, "Asymptotic tracking for systems with structured and unstructured uncertainties," in *IEEE Transactions on Control Systems Technology*, vol. 16, No. 2, 2008, pp. 373–379.

[39] P. Pellanda, P. Apkarian, and H. D. Tuan, "Missile autopilot design via a multi-channel lft/lpv control method," *Int. J. Robust Nonlinear Control*, vol. 12, pp. 1–20, 2002.

[40] Z. Qu and J. X. Xu, "Model-based learning controls and their comparisons using Lyapunov direct method," *Asian J. Control*, vol. 4(1), pp. 99–110, 2002.

[41] A. Serrani, A. Zinnecker, L. Fiorentini, M. Bolender, and D. Doman, "Integrated adaptive guidance and control of constrained nonlinear air-breathing hypersonic vehicle models," in *Proc. IEEE Am. Control Conf.*, June 2009.

[42] J. Shamma and M. Athans, "Gain scheduling: Potential hazards and possible remedies," *IEEE Control System Magazine*, vol. vol. 12, no. no. 3, pp. pp. 101–107, 1992.

[43] J. S. Shamma, "Gain-scheduling missile autopilot design using linear parameter varying transformations," *Journal of Guidance, Control and Dynamics*, vol. 16, no. 2, pp. 256–263, 1993.

[44] D. Sigthorsson, P. Jankovsky, A. Serrani, S. Yurkovich, M. Bolender, and D. Doman., "Robust linear output feedback control of an air-breathing hypersonic vehicle," *J. Guid. Contr. Dynam.*, vol. 31, No. 4, pp. 1052–1066, July 2008.

[45] M. Spillman, P. Blue, S. Banda, and L. Lee, "A robust gain-scheduling example using linear parameter-varying feedback," in *Proceedings of the IFAC 13th Triennial World Congress*, 1996, pp. 221–226.

[46] K. Åström, T. Hägglund, C. Hang, and W. Ho, "Automatic tuning and adaptation for PID controllers-a survey," *Control Eng. Pract.*, vol. 1, no. 4, pp. 669–714, 1993.

[47] L. F. Vosteen, "Effect of temperature on dynamic modulus of elasticity of some structural allows," in *Tech. Rep. 4348, Langley Aeronoutical Laboratory, Hampton, VA*, August 1958.

[48] S. A. W.A., "Strong stabilization of mimo systems: An lmi approach," in *Systems, Signals and Devices*, 2009.

[49] Q. Wang and R. F. Stengel, "Robust nonlinear control of a hypersonic aircraft," *J. Guid. Contr. Dynam.*, vol. 23, no. 4, pp. 577–585, 2000.

[50] Z. D. Wilcox, S. Bhat, R. Lind, and W. E. Dixon, "Control performance variation due to aerothermoelasticity in a hypersonic vehicle: Insights for structural design," in *Proc. AIAA Guid. Navig. Control Conf.*, August 2009.

[51] Z. D. Wilcox, W. MacKunis, S. Bhat, R. Lind, and W. E. Dixon, "Robust nonlinear control of a hypersonic aircraft in the presence of aerothermoelastic effects," in *Proc. IEEE Am. Control Conf.*, St. Louis, MO, June 2009, pp. 2533–2538.

[52] ——, "Lyapunov-based exponential tracking control of a hypersonic aircraft with aerothermoelastic effects," *J. Guid. Contr. Dynam.*, vol. 33, no. 4, Jul./Aug 2010.

[53] T. Williams, M. A. Bolender, D. B. Doman, and O. Morataya, "An aerothermal flexible mode analysis of a hypersonic vehicle," in *AIAA Paper 2006-6647*, Aug. 2006.

[54] B. Xian, D. M. Dawson, M. S. de Queiroz, and J. Chen, "A continuous asymptotic tracking control strategy for uncertain nonlinear systems," *IEEE Trans. Autom. Control*, vol. 49, no. 7, pp. 1206–1211, Jul. 2004.

[55] M. Yoshihiko, "Adaptive gain-scheduled H-infinity control of linear parameter-varying systems with nonlinear components," in *Proc. IEEE Am. Control Conf.*, Denver, CO, June 2003, pp. 208–213.

BIOGRAPHICAL SKETCH

Zach Wilcox grew up in Yarrow Point, a city just outside of Seattle, Washington, and lived there until moving to Florida to attend college in 2001. He received dual Bachelor of Science degrees from the University of Florida's Aerospace and Mechanical Engineering department in the spring of 2006. During his undergraduate work, Zach participated as a diver on UF's Men's Swimming Diving Team. In addition, he did research work for UF's Micro Air Vehicle (MAV) group and participated in International MAV competitions. He recieved his Masters of Science in Aerospace Engineering from University of Florida in the spring of 2008. His Doctoral studies were in the Nonlinear Controls and Robotics Group in the Department of Mechanical and Aerospace Engineering under the advisement of Dr. Dixon. He received his Ph.D. in Aerospace Engineering in August 2010.